information services
gwasanaethau gwybodaeth

Title: Persistent influence of precession on northern ice sheet variability since the early Pleistocene*

Authors:

Stephen Barker, School of Earth and Environmental Sciences, Cardiff University, UK barkers3@cf.ac.uk

Aidan Starr, School of Earth and Environmental Sciences, Cardiff University, UK aidan.m.starr@gmail.com

Jeroen van der Lubbe, Department of Earth Sciences, Vrije Universiteit Amsterdam, Netherlands h.j.l.vander.lubbe@vu.nl

Alice Doughty, School of Earth and Climate Sciences, University of Maine, USA alice.doughty@maine.edu

Gregor Knorr, Alfred Wegener Institute, Bremerhaven, Germany grgorknorr@hotmail.com

Stephen Conn, School of Earth and Environmental Sciences, Cardiff University, UK sgconn@gmail.com

Sian Lordsmith, School of Earth and Environmental Sciences, Cardiff University, UK golaucymru@gmail.com

Lindsey Owen, School of Earth and Environmental Sciences, Cardiff University, UK OwenL5@cardiff.ac.uk

Alexandra Nederbragt, School of Earth and Environmental Sciences, Cardiff University, UK NederbragtA@cardiff.ac.uk

Sidney Hemming, Lamont-Doherty Earth Observatory, Columbia University, USA sidney@ldeo.columbia.edu

Ian Hall, School of Earth and Environmental Sciences, Cardiff University, UK Hall@cardiff.ac.uk

Leah Levay, International Ocean Discovery Program, Texas A&M University, USA levay@iodp.tamu.edu

IODP Exp 361 Shipboard Scientific Party (See Supplementary Materials)

Persistent influence of precession on northern ice sheet variability since the early Pleistocene

One-sentence summary: Precession-driven mass wasting of northern ice sheets became synonymous with glacial termination during the MPT

Authors:

Stephen Barker[1*], Aidan Starr[1], Jeroen van der Lubbe[2], Alice Doughty[3], Gregor Knorr[4], Stephen Conn[1], Sian Lordsmith[1], Lindsey Owen[1], Alexandra Nederbragt[1], Sidney Hemming[5], Ian Hall[1], Leah Levay[6] and the IODP Exp 361 Shipboard Scientific Party[**]

[1] School of Earth and Environmental Sciences, Cardiff University, UK

[2] Department of Earth Sciences, Vrije Universiteit Amsterdam, Netherlands

[3] School of Earth and Climate Sciences, University of Maine, USA

[4] Alfred Wegener Institute, Bremerhaven, Germany

[5] Lamont-Doherty Earth Observatory, Columbia University, USA

[6] International Ocean Discovery Program, Texas A&M University, USA

[*] Corresponding author: barkers3@cf.ac.uk

[**] See Supplementary Materials

Abstract (125 words)

Before ~1M years ago, variations in global ice volume were dominated by changes in obliquity but the role of precession remains unresolved. Using a record of North Atlantic ice rafting spanning the last 1.7Myr, we find that the onset of ice rafting within a given glacial cycle (reflecting ice sheet expansion) consistently occurred during times of decreasing obliquity, while mass ice wasting (ablation) events were consistently tied to minima in precession. Furthermore our results suggest that the ubiquitous association between precession-driven mass wasting events and glacial termination is a unique feature of the mid/late Pleistocene. Before then, (increasing) obliquity alone was sufficient to end a glacial cycle, before losing its dominant grip on deglaciation with the southward extension of northern hemisphere ice sheets since ~1Ma.

Main text (3,499 words)

Glacial cycles of the mid to late Pleistocene (approximately the last 0.7Myr) were characterized by their long (~100kyr) duration and relatively abrupt (~10kyr) termination (*1*). Their ~100kyr periodicity has stimulated debate as to which orbital parameters (if any) are most important in driving glacial-interglacial (G-IG) variability, given that direct orbital forcing at this frequency (eccentricity) is negligible (*2*) (Fig. 1). However, there is growing consensus that both precession and obliquity play a role (at least in glacial termination) through their combined influence on summer insolation across northern high latitudes (*3-5*). Prior to the Mid Pleistocene Transition (MPT; 1.25-0.7Ma) the situation was, at face value, more straightforward; G-IG variability was dominated by ~41kyr cyclicity, reflecting the near-linear control of ice sheet growth and decay by changes in axial tilt (giving rise to stronger or weaker seasonality) (*6*). On the other hand, the lack of a clear precession signal in pre-MPT G-IG cyclicity makes little sense because precession plays a substantial role (dependent on the metric employed; Fig. 1) in modulating northern-hemisphere summer insolation, which is often considered to be the most important factor in the growth and decay of large continental ice sheets (*3, 7, 8*).

Building on this premise, Raymo, Lisiecki and Nisancioglu (*9*) proposed that the 'missing' precession signal expected in pre-MPT records of benthic foraminiferal $\delta^{18}O$ (a 1st order proxy for global ice volume) might be obscured by the equal and opposite effects of northern versus southern hemisphere ice sheet variability on mean ocean $\delta^{18}O$ i.e. the interhemispheric asymmetry of precession effectively cancelled out variations on this timescale in the record of global ice volume while equivalent variations in the obliquity band (which are in-phase between north and south) were amplified. The elegant proposition of (*9*) is ultimately testable; records of northern (and southern) ice sheet variability should display strong fluctuations on precession timescales.

3

Searching for precession in early Pleistocene ice sheet variability

To this end we have produced a record of ice rafted debris (IRD) accumulation from NE Atlantic ODP Site 983 (60.4°N, 23.6°W, 1983m; Fig. S1), extending the previous record (*10-12*) by 500kyr back to 1.7Ma (*13*). The complete record comprises 9,389 samples with an average temporal resolution of 181 years. We employ three independent approaches for age model construction (*13*). Firstly, we utilize the age model constructed by Lisiecki and Raymo (*14*) for ODP Site 983 as part of their benthic $\delta^{18}O$ stack (LR04). The LR04 age model was constructed by tuning to a target derived using a simple ice sheet model driven by June 21 insolation at 65°N (a signal dominated by precession; Fig. 1). This implies that any orbital frequencies present in records using the LR04 timescale should be detectable but also risks introducing frequencies that might not exist in nature. We therefore derive a second age model (U1476pMag; Fig. S2) based on the growing body of absolutely-dated magnetic polarity reversals and magnetic excursions (*15*) and a new record of benthic $\delta^{18}O$ from IODP Site U1476 in the western Indian Ocean (15.8°S, 41.8°E, 2166m) (*13*). The frequency of age constraints available for this approach is relatively low (Table S1), resulting in relatively large (mean 16kyr 1σ) age uncertainties (Fig. S3) (*13*). However, the calculated absolute offset between U1476pMag and LR04 over the last 1.8Myr averages only 6.6kyr (maximum 16kyr), suggesting good agreement between these two completely independent approaches. Finally, we derive a third timescale for our record based on the precession-tuned age model developed for 'Shackleton' site IODP U1385 (37.6°N, 10.1°W, 2578m) (*13, 16*). Although this model is also orbitally tuned, it is independent of LR04 and as such, provides a useful comparison (Figs. S4, S5).

The record of IRD accumulation from ODP Site 983 is shown in Figure 2. IRD accumulation is plotted on a log scale to highlight variations during periods of relatively low accumulation when ice sheets are small

4

(i.e. interglacial periods). It has been suggested (*9*) that the apparent absence of precession (and domination of obliquity) frequencies in pre-MPT records of ice rafting from the North Atlantic could be due to the fact that most ice rafting occurs during deglaciation, when rising sea level can destabilize marine-based ice sheets (i.e. iceberg calving rates on North Atlantic marine-based ice margins are controlled primarily by sea level and hence are expected to follow the sea level record even if land-based ice sheets themselves vary on different timescales). Indeed, we typically observe the highest levels of IRD accumulation during terminal events, when sea level is rising (Fig. S6; (*13*)). This leads to an apparent lag of IRD accumulation (non-log-transformed) behind sea level (in this case the LR04 stack) on G-IG timescales. On the other hand, we observe no such lag when comparing log IRD with the LR04 stack (*13*). In fact, we observe coherency between log IRD and the LR04 stack on G-IG (at ~41kyr and subsequently ~100kyr) timescales throughout the last 1.7Myr (Figs. 2, S17). We suggest this reflects the fact that, following peak interglacial conditions, ice rafting increases as ice sheets expand to form more extensive marine-based margins and we note (using an algorithm to identify the start and end of significant ice rafting during each glacial cycle (*13*)) that the onset of significant ice rafting tends to occur within a narrow range of benthic δ^{18}O (3.9±0.2‰, Fig. 2), and continues throughout much of the subsequent glacial period. We therefore conclude that our record of ice rafting (log IRD) reflects variations in the size and/or lateral extent of circum-NE Atlantic ice sheets rather than sea level per se. Specifically, although ice rafting always represents ice sheet ablation (via iceberg calving), we suggest that the increase in ice rafting following an interglacial reflects net growth/extension of ice sheets, while the end of ice rafting reflects ice sheet recession before the next interglacial.

We test for the presence of significant (>90% confidence level, CL) frequencies in our records of IRD and benthic δ^{18}O (plus the LR04 stack) for different intervals and age models using 3 methods (*13*) (Figs. 3, S12-S14): a multi-taper method (MTM) autoregressive -AR(1)- model (*17, 18*), an alternative spectral

5

noise estimation method (LOWSPEC (*18*)) and an MTM harmonic F-test, which is independent (to first order) of the first two (*18*). We also perform continuous wavelet transforms on each dataset to allow visualization of its temporal evolution (Fig. S16). In summary, while we find strong power in the obliquity band of NE Atlantic ice rafting before the MPT (1.7 to 1.25Ma), we observe no significant (>90% CL) peaks in the precession band prior to 1.25Ma. We note that some power in the precession band is observed using the U1385 age model (which extends back to 1.43Ma; Fig. 3) but no peaks in this range pass the various significance tests we apply (*13*) (Fig. S15). Recent work (*19*) suggests that traditional spectral analysis techniques may be too insensitive for isolating precession frequencies in pre-MPT records but we note that the methods we employ do identify significant (>90% CL) precession-like peaks (albeit with relatively low power) within the LR04 stack and the benthic δ^{18}O record from U1476 even on its absolute (non-orbitally tuned) U1476pMag age model (Fig. 3), which suggests (in agreement with ref (*19*)) that precession probably played some role in early Pleistocene benthic δ^{18}O variability, either through an influence on ice volume or deep ocean temperature. On the other hand, our results from spectral analysis suggest that circum-NE Atlantic ice sheets did not fluctuate strongly at precession frequencies before the MPT. Moreover, the accumulation of IRD at our site rarely falls to zero for more than a few thousand years (Figs. S8, S9), suggesting that marine-proximal ice sheet margins existed even during interglacial periods throughout the last 1.7Myr. Thus, it is unlikely we are missing a precession signal derived from purely terrestrial ice sheets. In summary, while we cannot rule out the prediction (*9*) that pre-MPT ice sheets varied strongly at precession frequencies, we find little evidence to support it. However, closer visual inspection of the IRD record reveals an alternative picture, as we discuss below.

Ice sheet ablation driven by precession

In Figure 4 the record of IRD is plotted on its three independent age models, together with the beginning and end of significant ice rafting for each glacial cycle as determined by our algorithm (Figs. S7-10) (*13*). Note that the end of ice rafting within a given cycle is defined as the end of the latest phase of significant ice rafting lasting 2,800 years (*13*) or more prior to the subsequent interglacial (defined as a minimum in LR04 δ^{18}O with absolute value <4.25‰ (*13*)). This is because we wish to identify the major ice rafting events (i.e. mass ablation events) that are characteristic of mid/late Pleistocene glacial terminations (*11, 20, 21*). For our purposes, we name these 'terminal ice rafting' (TIR) events, meaning that they represent the last major episode of ice rafting within a glacial cycle, even if (as we describe below) they do not always coincide with the transition to interglacial conditions.

In Figure 5 we assess the start and end of ice rafting with respect to the phase of precession and obliquity. We find a consistent link between TIR events and precession over the last 1.7Myr (Table S2), with the end of TIR events occurring on average 0.2 ± 2.4kyr (95% CI, when combining events from the three age model approaches (*13*)) before minima in precession prior to 1Ma and 0.9 ± 2.0kyr behind precession minima since 1Ma. Combining all instances we find that TIR events ended on average 0.5 ± 1.5kyr behind minima in precession over the last 1.7Myr. Since TIR events are (by our definition) 2.8kyr or more in duration, our findings imply that large-scale ablation of northern ice sheets typically coincided with increasing to maximum summer insolation as a function of precession throughout the last 1.7Myr. Notably this conclusion could not be drawn using traditional spectral analytical techniques, which are designed to detect periodic waveforms rather than the timing of discrete events.

A different relationship is observed with obliquity (Table S2). Before 1Ma, TIR events tended to end while obliquity was increasing (ending on average 8.3 ± 2.4kyr before a peak in obliquity; Fig. 5) but since 1Ma, their ending has been more closely aligned with maxima in obliquity (offset = 0.3 ± 3.4kyr;

7

Fig. 5). On the other hand, deglacial transitions in benthic $\delta^{18}O$ have been closely aligned with maxima in obliquity throughout the last 1.7Myr (average offset between mid-point of deglaciation and maximum obliquity = 2.3 ± 1.7kyr; Fig. S11) (*13*). The association of post-MPT TIR events with insolation maxima as a function of both obliquity and precession (as described above) provides additional support for a dual role of obliquity and precession in driving mid/late Pleistocene glacial terminations (*4*). However, the situation seems to have been different before that time.

Terminal ice rafting events and deglaciation

Our results suggest that precession has played a persistent role in TIR events since the early Pleistocene. However, before 1Ma those events were not always aligned with deglacial transitions according to benthic $\delta^{18}O$ (Fig.6); Over the last 1Myr the end of TIR events corresponded closely with the latter half of deglaciation as defined by the corresponding decrease in benthic $\delta^{18}O$ (Fig. 6C) i.e. mass ice sheet wasting coincided with the transition to interglacial conditions. Prior to 1Ma, however, TIR events tended to end earlier with respect not only to obliquity (Fig. 5) but also to deglaciation as constrained by benthic $\delta^{18}O$ (Fig. 6C, Table S2; note this result is insensitive to the age model employed). Barker *et al*. (*12*) identified a termination-like event (T14.1 in Fig. 4) ~1.05Ma within Marine Isotope Stage (MIS) 30. While it was conceded that T14.1 could not be a true termination in the sense that it did not coincide with decreasing benthic $\delta^{18}O$, the event notably bore other hallmarks of late Pleistocene terminations, including widespread ice rafting followed by an abrupt warming across the NE Atlantic. It was also noted that TIR event T14.1 was aligned with a maximum in northern-hemisphere summer insolation that was a function of precession (i.e. a minimum in the precession parameter) and not obliquity.

Our record suggests that this pattern was relatively common before 1Ma. In fact, prior to that time TIR events commonly ended before the decrease in benthic $\delta^{18}O$ typically taken to represent deglaciation (Fig. 6C). Our results therefore suggest that prior to 1Ma, TIR events were not synonymous with deglaciation (the transition to interglacial conditions). Furthermore, whether or not a TIR event coincided (or even overlapped) with deglaciation before 1Ma depended on the phasing between obliquity and precession, as we discuss below.

In Figure 6D we plot the temporal offset between the mid-point of each deglaciation and the end of its associated TIR event versus the offset between the obliquity peak closest to that deglaciation and its nearest minimum in precession. Throughout the last 1.7Myr the end of a TIR event tended to coincide (within a few kyr) with the mid-point of deglaciation when the closest precession minimum occurred prior to the peak in obliquity (a negative obliquity-precession offset in Fig. 6, e.g. events ii and iii). On the other hand, since 1Ma, when the closest precession minimum occurred after the peak in obliquity (a positive obliquity-precession offset in Fig. 6, e.g. event i) the TIR event (more often than not) continued beyond the mid-point of deglaciation (Fig. 6D), presumably driven by the precession minimum directly following the maximum in obliquity (Fig. 6E). Moreover, before 1Ma, the same positive obliquity-precession offset typically produced a TIR event that ended up to 10-20kyr before the mid-point of deglaciation (Fig. 6D, e.g. events iv and v), apparently driven by the preceding minimum in precession (Fig. 6E). Thus, since 1Ma, TIR events have always coincided with deglacial transitions but prior to 1Ma, a TIR event might start and end before deglaciation had even begun, if the obliquity-precession offset was positive.

The decoupling observed between TIR events and deglaciation prior to 1Ma suggests that while obliquity may have been responsible for the majority of deglacial ice sheet ablation prior to the MPT,

the most conspicuous ice rafting events (at least across the NE Atlantic) were a result of precession forcing. We suggest this reflects the difference between precession and obliquity in their influence on the spatiotemporal distribution of insolation (Fig. 1); while obliquity has a greater effect on integrated summer energy over higher latitudes (which could explain its dominant control on the net waxing and waning of high latitude ice sheets prior to the MPT), precession drives larger changes in the intensity of peak summer warmth at lower latitudes, which could explain why it is so effective at driving massive iceberg calving events along the southern margins of large ice sheets (even if these had little impact on the overall volume of land-based ice prior to 1Ma).

Our results therefore imply a change in the influence of obliquity over deglaciation across the MPT. Specifically, before 1Ma, ice sheets were apparently unable to survive a maximum in obliquity such that a subsequent minimum in precession would have little left to melt (in terms of marine-terminating ice sheets) thus the preceding precession-driven ablation event (that occurred when ice sheets were still large; Fig. 6E) was the last within that cycle. After 1Ma, sufficient ice apparently remained even after the peak in obliquity associated with deglaciation, such that a subsequent minimum in precession could drive further ablation and ice rafting. In summary, it seems that precession minima will always drive ice ablation events if sufficient ice exists and whether or not this is the case depends on the influence of obliquity over deglaciation, which weakened across the MPT. Such a change implies the growth of larger northern hemisphere ice sheets since ~1Ma (which required more energy to melt e.g. (*5*)) and/or their net migration towards lower latitudes, where the effects of obliquity are weaker and those of precession stronger (Fig. 1). In turn this could reflect the proposed net increase in flux of Atlantic surface waters entering the Nordic Seas (the Atlantic Inflow) since ~1.2Ma, promoting enhanced moisture transport and the growth of larger ice sheets with an increasingly southern influence (*12*).

A notable exception to the 'pre-1Ma' pattern described above occurred ~1.2Ma (Fig. 4). Although TIR event T17 coincided with the deglacial transition into MIS 35, neither event was associated with a maximum in obliquity (according to two out of the three age models we employ), occurring instead on the next downward limb of obliquity and coincident with a minimum in precession ~1.19Ma. Moreover (and according to all three age models) the subsequent minimum in obliquity (~1.18Ma) was the only minimum in the past 1.7Myr not to have been associated with the onset or continuation of significant ice rafting (Fig. 2), which we suggest could reflect the late occurrence of T17. Ultimately the result was the appearance of glacial cycles substantially exceeding ~41kyr in duration (Figs. 3, 4), marking the weakening grip of obliquity on G-IG variability and the beginning of the MPT.

We suggest that our observation of a direct link between the temporal offset of TIR events versus deglaciation and the phasing of obliquity versus precession (Fig. 6) provides the strongest evidence yet for the influence of precession -in addition to obliquity- on ice sheet variability during the early Pleistocene. This is highlighted by a test for significance of the relationship >1Ma (Fig. 6D). Using the surrogateCor function in Astrochron (*22*) we obtain a correlation coefficient of -0.73 (p<0.005) (*13*), meaning we can state with confidence that the timing of TIR events versus deglaciation prior to 1Ma was related to the phase of precession with respect to obliquity.

Pre-MPT precession signal obscured by obliquity

Based on a detailed study of the last 0.8Myr, Tzedakis and colleagues (*23*) concluded that glacial inception (the start of a glacial period) is strongly tied to periods of decreasing obliquity, emphasizing the importance of milder northern-hemisphere summers (and winters) for the growth and survival of terrestrial ice masses at high latitudes. Our results extend that conclusion to the past 1.7Myr; the onset

of significant ice rafting (implying that ice sheets have grown large enough to develop extensive marine-based margins) is aligned with decreasing to low obliquity in almost all cases (Fig. 5). Conversely our results do not allow us to determine an unambiguous link between precession and the onset of ice rafting (Fig. 5).

Because decreasing obliquity appears to be critical for glacial inception, this places an upper limit of 1/41kyr on the frequency of glacial cycles throughout the last 1.7Myr (a possible exception is the interval of high frequency -precession-like- variability ~1Ma when three 'inception' events occurred across two obliquity cycles; Fig. 2). Hence although our results suggest that precession has played a persistent role in the ablation of marine terminating ice sheets since 1.7Ma, we should not be surprised by the lack of a strong precession signal in the frequency domain of pre-MPT G-IG variability.

Emergence of glacial terminations across the MPT

The global impacts related to TIR events during the mid to late Pleistocene are well documented, for example abrupt shifts in ocean circulation (*11, 20*), changing greenhouse gas concentrations (*11, 24*) and global precipitation patterns (*24, 25*) are all thought to occur in tandem with major North Atlantic ice rafting during glacial termination. Our results suggest that these impacts may also have been prevalent in the ~41kyr world. For example, we observe features within the records of benthic foraminiferal δ^{18}O and δ^{13}C from IODP Site U1476 that match the timing of major IRD events at Site 983 including some that did not lead directly to deglaciation (Fig. 4). The record of δ^{18}O from Site U1476 itself displays an excellent correlation with the LR04 stack (*13*) suggesting that it represents a reasonable reflection of global mean ocean composition. Thus, the commonality between such distal and diverse proxy records (between IRD accumulation in the North Atlantic and proxies for deep ocean chemistry and circulation

12

in the Indian Ocean; Fig. S1) attests to the wider significance of our record from Site 983 i.e. the events we record are probably not just a local phenomenon.

Our results therefore suggest that precession-driven mass ice ablation events have occurred since the early Pleistocene, with related effects on a global scale. On the other hand, their ubiquitous association with deglaciation is a phenomenon unique to the mid/late Pleistocene. Specifically, we suggest that prior to the MPT, obliquity alone was sufficient to end a glacial cycle (as evidenced by the fact that subsequent peaks in precession did not drive further ablation). However, since then all deglaciations have been associated with precession-driven mass ablation events, which we attribute to the increased importance of precession for melting the larger proportion of northern hemisphere ice sheets situated at lower latitudes since the MPT. We therefore recommend that the term glacial termination (sensu stricto) be reserved for deglaciations of the mid to late Pleistocene, which involve the mutual interplay between maxima and minima in obliquity and precession, respectively.

References and Notes

1.   W. S. Broecker, J. van Donk, Insolation changes, ice volumes and the O^{18} in deep-sea cores. *Reviews of Geophysics and Space Physics* **8**, 169-198 (1970).

2.   J. Imbrie, A. Berger, E. A. Boyle, S. C. Clemens, A. Duffy, W. R. Howard, G. Kukla, J. Kutzbach, D. G. Martinson, A. McIntyre, A. C. Mix, B. Molfino, J. J. Morley, L. C. Peterson, N. G. Pisias, W. L. Prell, M. E. Raymo, N. J. Shackleton, J. R. Toggweiler, On the structure and origin of major glaciation cycles 2. the 100,000-year cycle. *Paleoceanography* **8**, 699-735 (1993).

3.   M. Milankovitch, *Kanon der Erdbestrahlung und seine Andwendung auf das Eiszeiten-problem*. (Royal Serbian Academy, Belgrade, 1941).

4.   P. Huybers, Combined obliquity and precession pacing of late Pleistocene deglaciations. *Nature* **480**, 229-232 (2011).

5.   P. Tzedakis, M. Crucifix, T. Mitsui, E. W. Wolff, A simple rule to determine which insolation cycles lead to interglacials. *Nature* **542**, 427-432 (2017).

6.   J. Imbrie, E. A. Boyle, S. C. Clemens, A. Duffy, W. R. Howard, G. Kukla, J. Kutzbach, D. G. Martinson, A. McIntyre, A. C. Mix, B. Molfino, J. J. Morley, L. C. Peterson, N. G. Pisias, W. L. Prell, M. E. Raymo, N. J. Shackleton, J. R. Toggweiler, On the Structure and Origin of Major Glaciation Cycles 1. Linear responses to Milankovitch forcing. *Paleoceanography* **7**, 701-738 (1992).

7.   J. Imbrie, J. Z. Imbrie, Modeling the Climatic Response to Orbital Variations. *Science* **207**, 943-953 (1980).

8.   M. E. Raymo, K. Nisancioglu, The 41 kyr world: Milankovitch's other unsolved mystery. *Paleoceanography* **18**, (2003).

9.   M. E. Raymo, L. E. Lisiecki, K. H. Nisancioglu, Plio-pleistocene ice volume, Antarctic climate, and the global delta O-18 record. *Science* **313**, 492-495 (2006).

10.   S. Barker, J. Chen, X. Gong, L. Jonkers, G. Knorr, D. Thornalley, Icebergs not the trigger for North Atlantic cold events. *Nature* **520**, 333-336 (2015).

11.   S. Barker, G. Knorr, S. Conn, S. Lordsmith, D. Newman, D. Thornalley, Early interglacial legacy of deglacial climate instability. *Paleoceanography and Paleoclimatology*, (2019).

12.   S. Barker, X. Zhang, L. Jonkers, S. Lordsmith, S. Conn, G. Knorr, Strengthening Atlantic Inflow across the Mid-Pleistocene Transition. *Paleoceanography and Paleoclimatology*, e2020PA004200 (2021).

13.   See Supplementary Materials.

14.   L. E. Lisiecki, M. E. Raymo, A Pliocene-Pleistocene stack of 57 globally distributed benthic δ^{18}O records. *Paleoceanography* **20**, DOI:10.1029/2004PA001071 (2005).

15.   J. E. Channell, B. S. Singer, B. R. Jicha, Timing of Quaternary geomagnetic reversals and excursions in volcanic and sedimentary archives. *Quaternary Science Reviews* **228**, 106114 (2020).

16.   D. Hodell, L. Lourens, S. Crowhurst, T. Konijnendijk, R. Tjallingii, F. Jiménez-Espejo, L. Skinner, P. Tzedakis, S. S. P. Members, A reference time scale for Site U1385 (Shackleton Site) on the SW Iberian Margin. *Global and Planetary Change* **133**, 49-64 (2015).

17.   M. E. Mann, J. M. Lees, Robust estimation of background noise and signal detection in climatic time series. *Climatic change* **33**, 409-445 (1996).

18.   S. R. Meyers, Seeing red in cyclic stratigraphy: Spectral noise estimation for astrochronology. *Paleoceanography* **27**, (2012).

19.   P. R. Liautaud, D. A. Hodell, P. J. Huybers, Detection of significant climatic precession variability in early Pleistocene glacial cycles. *Earth and Planetary Science Letters* **536**, 116137 (2020).

20.   K. A. Venz, D. A. Hodell, C. Stanton, D. A. Warnke, A 1.0 Myr record of glacial North Atlantic intermediate water variability from ODP site 982 in the northeast Atlantic. *Paleoceanography* **14**, 42-52 (1999).

21.   S. Barker, G. Knorr, Millennial scale feedbacks determine the shape and rapidity of glacial termination. *Nature Communications* **12**, 2273 (2021).

22.   S. R. Meyers, Astrochron: An R Package for Astrochronology. http://cran.r-project.org/package=astrochron (2014).

23.   P. Tzedakis, E. Wolff, L. Skinner, V. Brovkin, D. Hodell, J. F. McManus, D. Raynaud, Can we predict the duration of an interglacial? *Climate of the Past* **8**, 1473-1485 (2012).

24.   L. Loulergue, A. Schilt, R. Spahni, V. Masson-Delmotte, T. Blunier, B. Lemieux, J. M. Barnola, D. Raynaud, T. F. Stocker, J. Chappellaz, Orbital and millennial-scale features of atmospheric CH_4 over the past 800,000 years. *Nature* **453**, 383-386 (2008).

25. H. Cheng, R. L. Edwards, A. Sinha, C. Spötl, L. Yi, S. Chen, M. Kelly, G. Kathayat, X. Wang, X. Li, The Asian monsoon over the past 640,000 years and ice age terminations. *Nature* **534**, 640-646 (2016).

26. A. Berger, M. F. Loutre, Insolation Values for the Climate of the Last 10 Million Years. *Quaternary Science Reviews* **10**, 297-317 (1991).

27. E. Jansen, M. E. Raymo, P. Blum, *Proceedings of the Ocean Drilling Program, Initial Reports. Vol. 162*. (Texas A & M University, Ocean Drilling Program, 1996).

28. I. Hall, S. Hemming, L. LeVay, S. Barker, M. Berke, L. Brentegani, T. Caley, A. Cartagena-Sierra, C. Charles, J. Coenen, in *Proceedings of the International Ocean Discovery Program, 361*. (International Ocean Discovery Program, 2017).

29. G. Bond, H. Heinrich, W. Broecker, L. Labeyrie, J. McManus, J. Andrews, S. Huon, R. Jantschik, S. Clasen, C. Simet, K. Tedesco, M. Klas, G. Bonani, S. Ivy, Evidence for massive discharges of icebergs into the north Atlantic Ocean during the Last Glacial Period. *Nature* **360**, 245-249 (1992).

30. G. C. Bond, R. Lotti, Iceberg Discharges into the North-Atlantic on Millennial Time Scales During the Last Glaciation. *Science* **267**, 1005-1010 (1995).

31. H. J. L. v. d. Lubbe, I. R. Hall, S. Barker, S. R. Hemming, J. Just, T. F. Baars, A. Starr, J. C. A. Joordens, Shipboard_scientists, Invigoration of Indian Ocean zonal circulation drove Pleistocene eastern Africa aridification in review (2021).

32. B. S. Singer, A Quaternary geomagnetic instability time scale. *Quaternary Geochronology* **21**, 29-52 (2014).

33. J. Channell, C. Xuan, D. Hodell, Stacking paleointensity and oxygen isotope data for the last 1.5 Myr (PISO-1500). *Earth and Planetary Science Letters* **283**, 14-23 (2009).

34.   J. E. T. Channell, D. A. Hodell, B. Lehman, Relative geomagnetic paleointensity and delta O-18 at ODP Site 983 (Gardar Drift, North Atlantic) since 350 ka. *Earth and Planetary Science Letters* **153**, 103-118 (1997).

35.   J. E. T. Channell, H. F. Kleiven, Geomagnetic palaeointensities and astrochronological ages for the Matuyama-Brunhes boundary and the boundaries of the Jaramillo Subchron: palaeomagnetic and oxygen isotope records from ODP Site 983. *Philosophical Transactions of the Royal Society of London Series a-Mathematical Physical and Engineering Sciences* **358**, 1027-1047 (2000).

36.   I. R. Hall, S. R. Hemming, L. J. LeVay, S. R. Barker, M. A. Berke, L. Brentegani, T. Caley, A. Cartagena-Sierra, C. D. Charles, J. J. Coenen, Proceedings of the International Ocean Discovery Program; South African climates (Agulhas LGM density profile); Expedition 361 of the riserless drilling platform, Port Louis, Mauritius, to Cape Town, South Africa; Sites U1474-U1479, 30 January-31 March 2016. (2017).

37.   H. J. L. van der Lubbe, I. R. Hall, S. Barker, S. R. Hemming, T. F. Baars, A. Starr, J. Just, B. C. Backeberg, J. C. A. Joordens, Indo-Pacific Walker circulation drove Pleistocene African aridification. *Nature* **598**, 618-623 (2021).

38.   B. C. Lougheed, S. Obrochta, A Rapid, Deterministic age-depth modeling routine for geological sequences with inherent depth uncertainty. *Paleoceanography and Paleoclimatology* **34**, 122-133 (2019).

39.   L. B. Railsback, P. L. Gibbard, M. J. Head, N. R. G. Voarintsoa, S. Toucanne, An optimized scheme of lettered marine isotope substages for the last 1.0 million years, and the climatostratigraphic nature of isotope stages and substages. *Quaternary Science Reviews* **111**, 94-106 (2015).

40.   P. Berens, CircStat: a MATLAB toolbox for circular statistics. *J Stat Softw* **31**, 1-21 (2009).

41.	R_Core_Team, R: A Language and Environment for Statistical Computing. *R Foundation for Statistical Computing* **Vienna, Austria**, https://www.R-project.org/ (2020).

42.	D. J. Thomson, Spectrum estimation and harmonic analysis. *Proceedings of the IEEE* **70**, 1055-1096 (1982).

43.	D. B. Percival, A. T. Walden, *Spectral analysis for physical applications*. (cambridge university press, 1993).

44.	A. Grinsted, J. C. Moore, S. Jevrejeva, Application of the cross wavelet transform and wavelet coherence to geophysical time series. *Nonlinear processes in geophysics* **11**, 561-566 (2004).

45.	D. Maraun, J. Kurths, Cross wavelet analysis: significance testing and pitfalls. *Nonlinear Processes in Geophysics* **11**, 505-514 (2004).

46.	M. Crucifix, Palinsol: insolation for palaeoclimate studies, R package version 0.93. https://bitbucket.org/mcrucifix/insol (2016).

47.	J. Laskar, P. Robutel, F. Joutel, M. Gastineau, A. C. M. Correia, B. Levrard, A long-term numerical solution for the insolation quantities of the Earth. *Astronomy & Astrophysics* **428**, 261-285 (2004).

48.	R. A. Locarnini, A. V. Mishonov, J. I. Antonov, T. P. Boyer, H. E. Garcia, O. K. Baranova, M. M. Zweng, D. R. Johnson, in *NOAA Atlas NESDIS 68,* S. Levitus, Ed. (U.S. Government Printing Office, Washington, D.C., 2010), pp. 184.

49.	M. E. Raymo, D. W. Oppo, B. P. Flower, D. A. Hodell, J. F. McManus, K. A. Venz, K. F. Kleiven, K. McIntyre, Stability of North Atlantic water masses in face of pronounced climate variability during the Pleistocene. *Paleoceanography* **19**, PA2008, doi:10.1029/2003PA000921 (2004).

50.	H. F. Kleiven, I. R. Hall, I. N. McCave, G. Knorr, E. Jansen, Coupled deep-water flow and climate variability in the middle Pleistocene North Atlantic. *Geology* **39**, 343-346 (2011).

Acknowledgements

List of Supplementary Materials

IODP Exp 361 Shipboard Scientific Party information
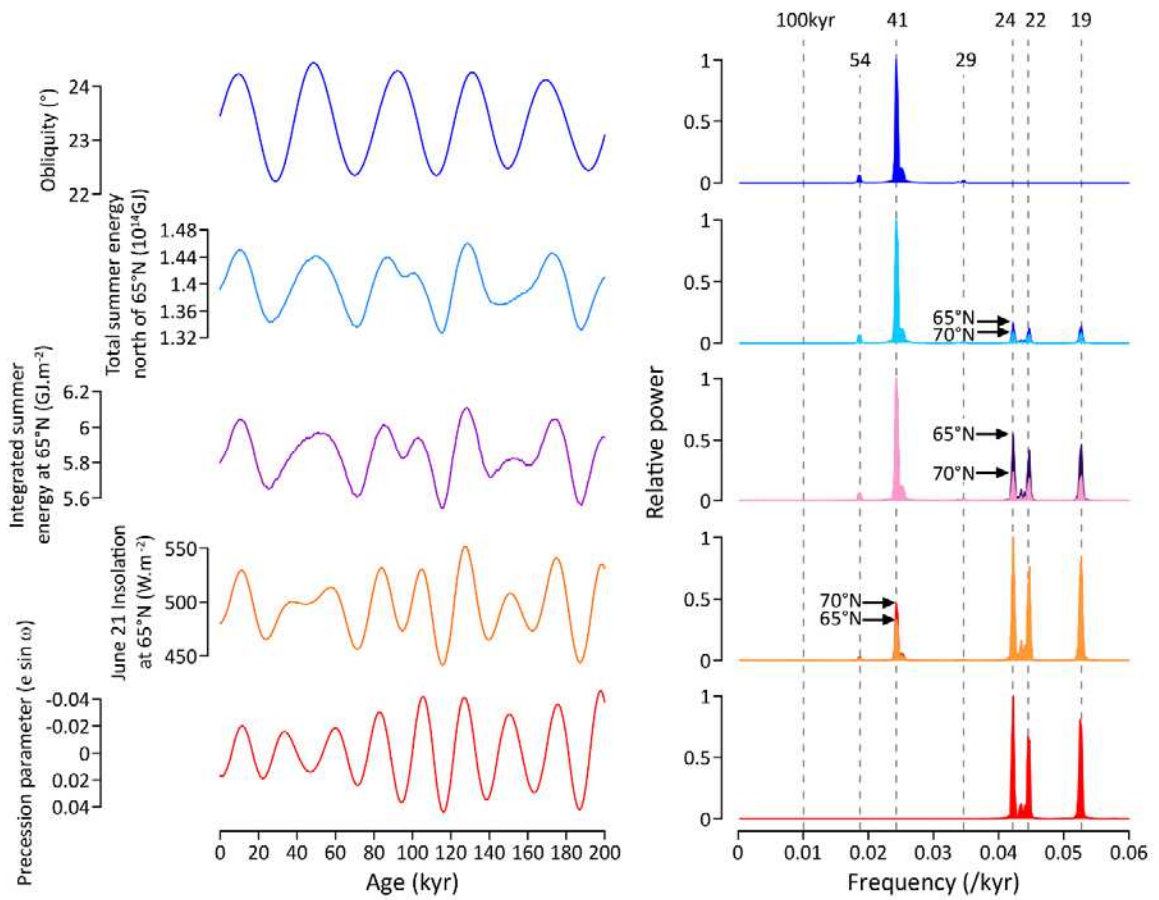
Materials and Methods

Tables S1, S2

Figs. S1 – S17

Supplementary Dataset S1

Matlab files.zip

**Figures and Legends:** See following pages

Figure 1. Influence of obliquity and precession on the spatiotemporal distribution of incoming solar radiation. Left: variations in axial tilt (obliquity) and precession (*26*) with various metrics for assessing changes in northern summer insolation (*13*). Note that a negative value of the precession parameter is associated with a positive anomaly in northern hemisphere summer insolation. Right: power spectra for obliquity, precession and insolation metrics at 2 different latitudes. All metrics display significant (>99% CL according to the various tests outlined by (*18*)) power in the obliquity and precession bands with increasing power in the precession band relative to obliquity at lower latitudes. Power spectra are

normalized to the maximum power in each case. Vertical dotted lines in right panel are expected orbital

periods in kyr (note no metric displays substantial power at ~100kyr).
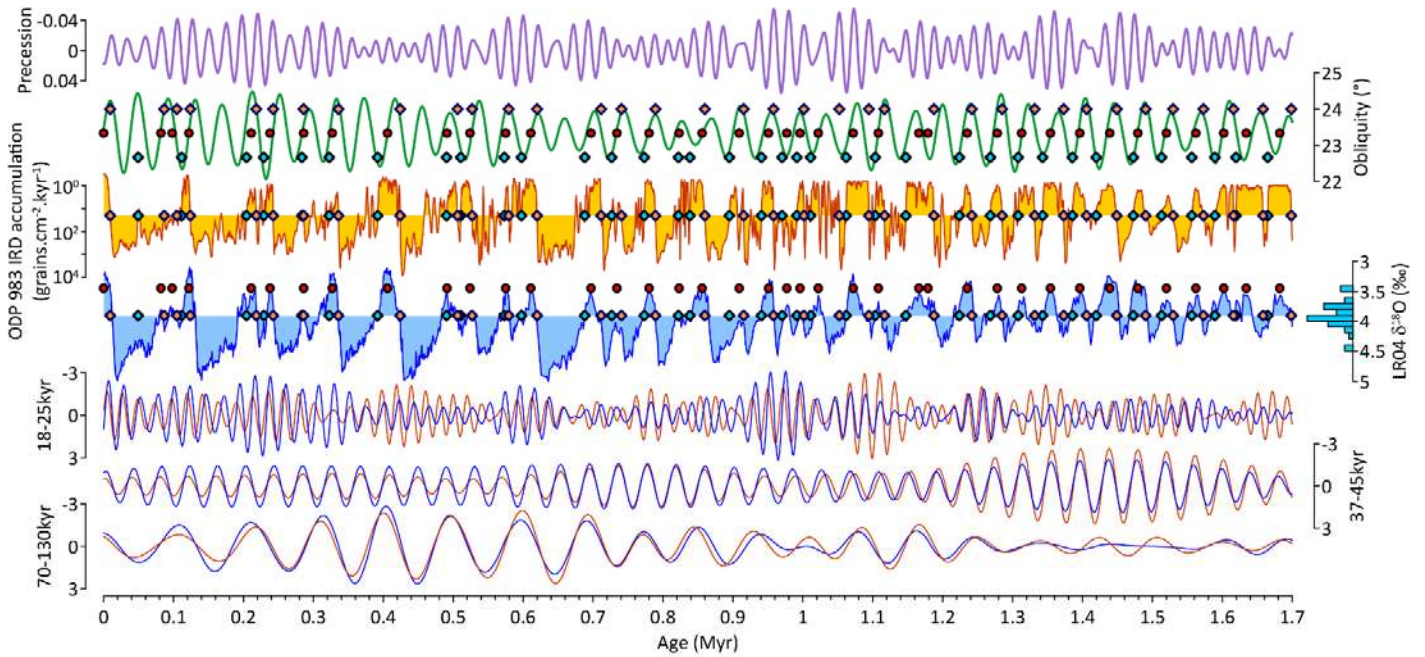
Figure 2. 1.7Myr of ice rafting across the NE Atlantic. Throughout: red circles are interglacials (as determined by our algorithm (*13*)), blue diamonds represent onset of significant ice rafting (see orange-filled curve), orange diamonds represent end of TIR events (*13*). From top to bottom: precession (*26*), obliquity (*26*), IRD accumulation from ODP 983 on the LR04 age model (data have been smoothed and detrended to highlight intervals of significant ice rafting (*13*)), LR04 benthic stack (histogram represents values of $\delta^{18}O$ at time of each IRD onset, mean=3.9±0.2‰ as indicated by horizontal fill threshold of LR04 curve), 18-25kyr, 37-45kyr and 70-130kyr filter outputs of log IRD (red) and LR04 stack (blue). Note coherence between LR04 stack and log IRD on G-IG (41kyr and subsequently ~100kyr) timescales throughout the last 1.7Myr (see also Fig. S17).
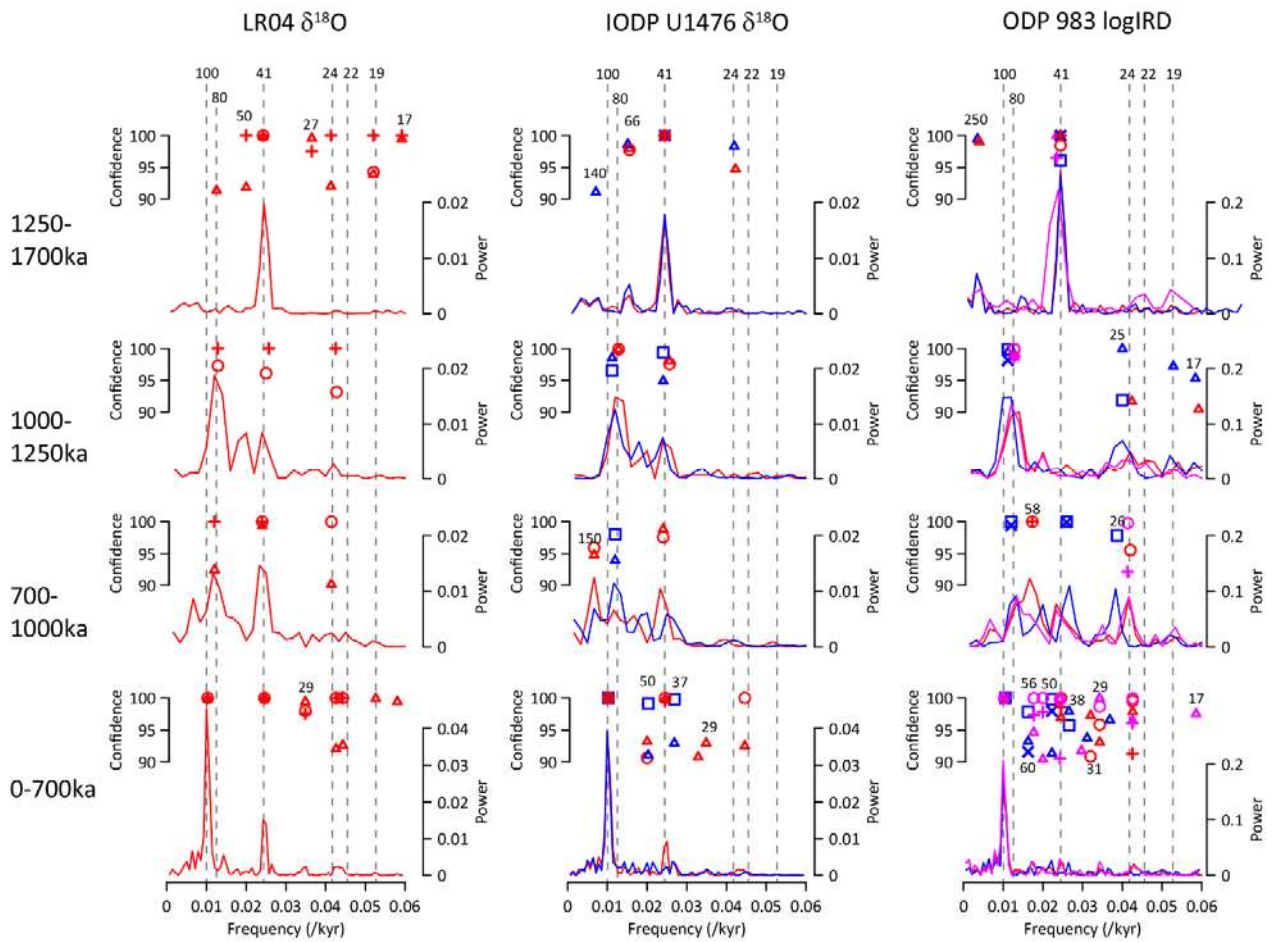
Figure 3. No significant precession periodicity in pre-MPT ice rafting. Illustrative power spectra and significant spectral peaks identified in LR04, U1476 benthic δ^{18}O and ODP 983 log IRD for 4 distinct time windows using 3 timescales and 3 different spectral methods. Red, blue and magenta represent LR04, U1476pMag and U1385 timescales respectively. Circles and squares represent results using LOWSPEC (*13, 18*), crosses and exes use the robust AR1 method (*17, 18*) and triangles represent the MTM harmonic F-test (*13*). No statistically significant (>90% CL) precession-like peaks are identified in the pre-MPT (1250-1700ka) section of log IRD while they are present in records of benthic δ^{18}O.
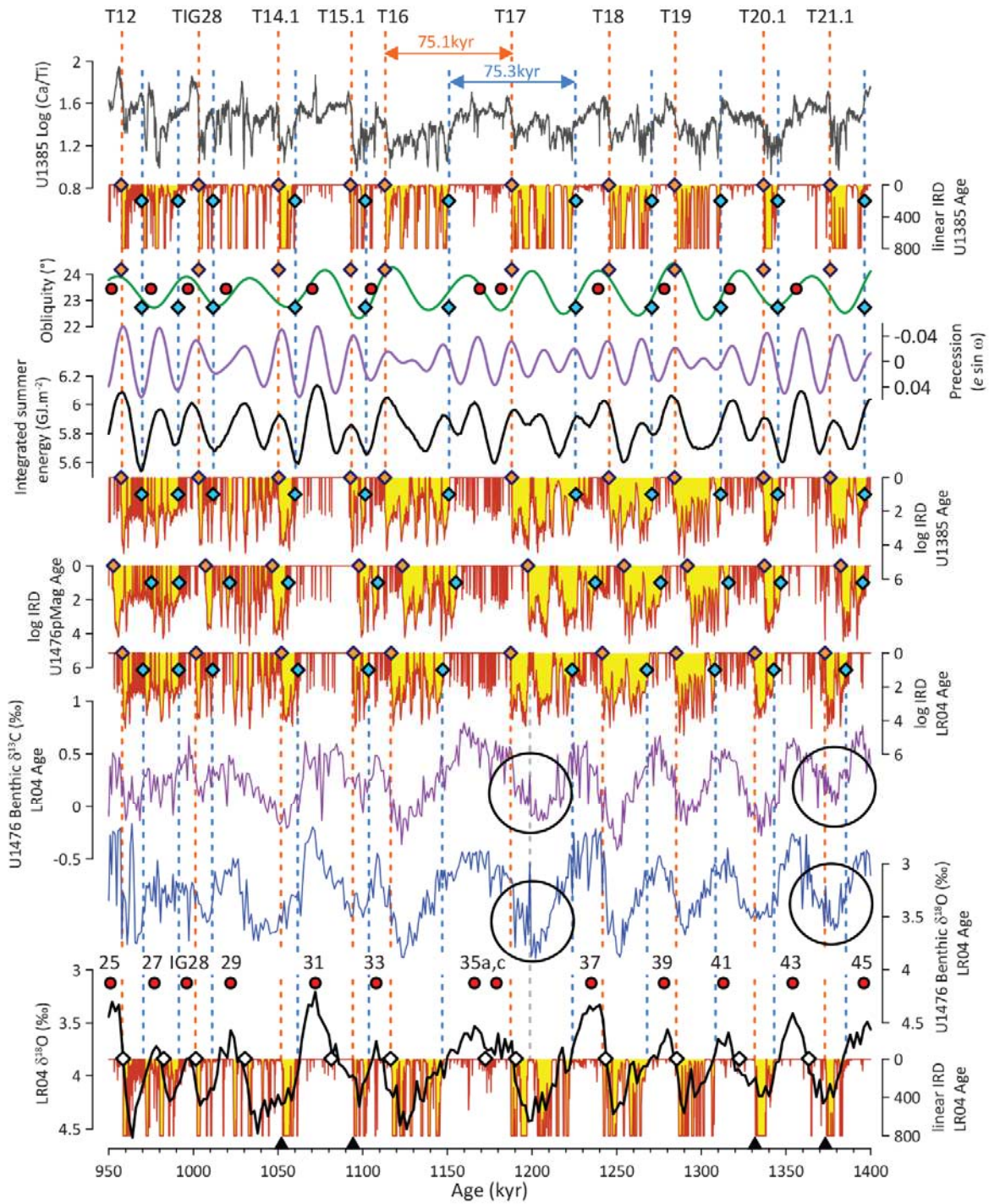
Figure 4. Obliquity loses grip on deglaciation. Throughout: red circles are interglacials (numbered; IG28

is a minimum in δ^{18}O associated with MIS 28 (*12*)), white diamonds are deglacial transitions with respect

to δ^{18}O (*13*), blue diamonds and vertical dashed lines represent onset of significant ice rafting, orange diamonds (and lines) represent end of TIR events. Orange and blue double-headed arrows highlight lengthening of glacial cycles to approximate multiples of the obliquity period following the late occurrence of T17 (see text and also Fig. 3; 1000-1250ka window). From top to bottom: log (Ca/Ti) from U1385 (*16*), ODP 983 IRD accumulation on linear scale (note cropped scale), obliquity and precession (*26*), integrated summer energy at 65°N, log IRD from ODP 983 on U1385, U1476pMag and LR04 age models, benthic foraminiferal δ^{13}C and δ^{18}O from U1476 on its LR04 age model (*13*), the LR04 stack (*14*) and linear IRD on its LR04 age model. Black triangles at bottom highlight 'non-terminating' TIR events (identified as T14.1, T15.1 etc). Large black circles highlight shifts toward lighter values of benthic δ^{18}O in U1476 within glacial intervals. Both of these shifts are aligned with coincident features in the records of benthic δ^{13}C and IRD. Note our algorithm does not assign a TIR event for T13 because IRD accumulation does not subside sufficiently before MIS 27.
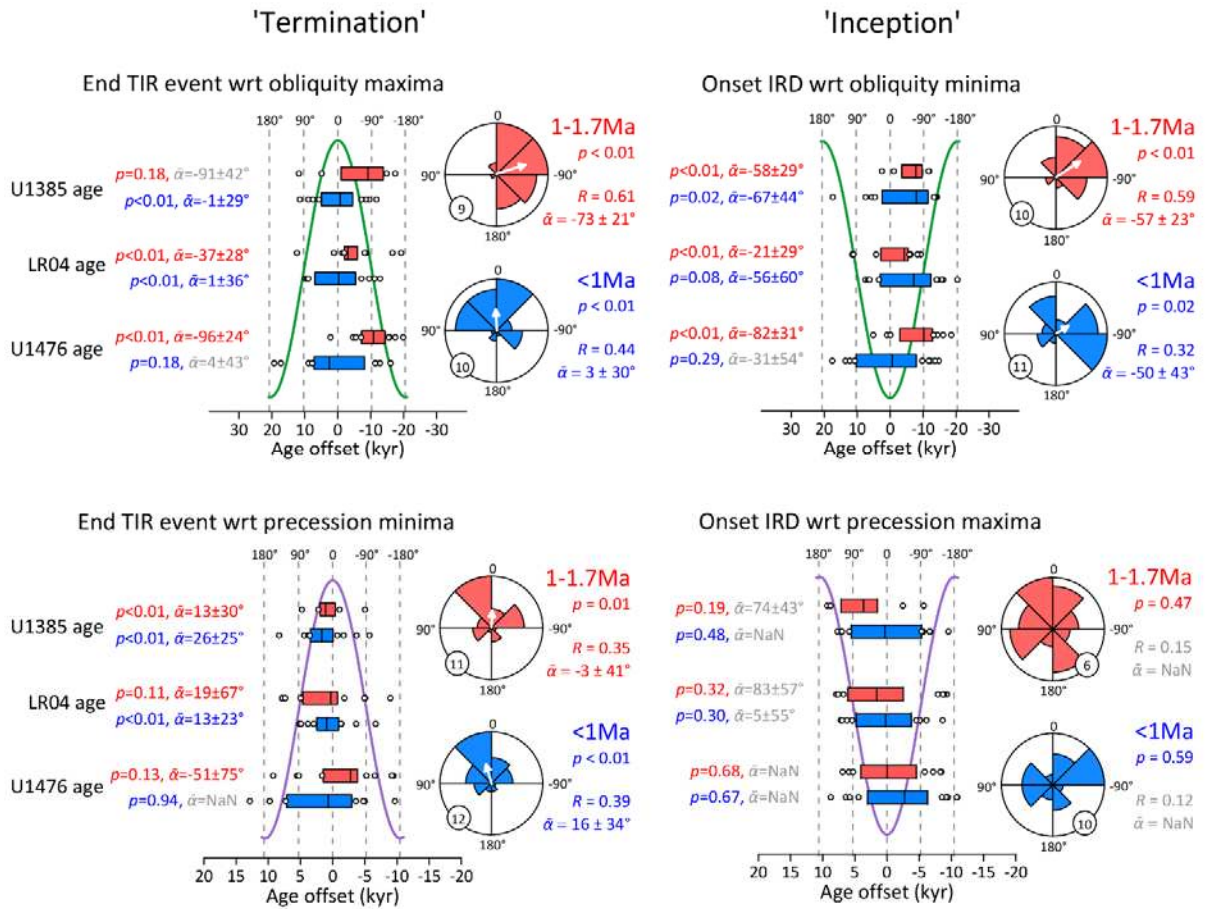
Figure 5. Precession drives terminal ice rafting events throughout last 1.7Myr. Onset (end) of North Atlantic ice rafting across glacial cycles of the past 1.7Myr with respect to insolation minima (maxima) as a function of obliquity and precession (note precession minima imply insolation maxima -and vice versa- in northern hemisphere). All curves represent idealized cycles of obliquity (41kyr period; green) or precession (21kyr period; purple). Box plots for each age model represent median and interquartile range, all other data-points are shown. Red and blue colors represent pre- and post-1Ma. Rose diagrams combine results from the 3 age models (*13*): Lower values of *p* suggest higher likelihood of a non-uniform distribution, *R* is mean resultant vector (*R*→1 as data converge), ᾱ is mean direction with 95% confidence interval or 80% CI (grey text) for *p*>0.15 (NaN is returned for *p*>0.4). Direction of white arrow = ᾱ, length = *R**radial axis. Circled number is length of radial axis.
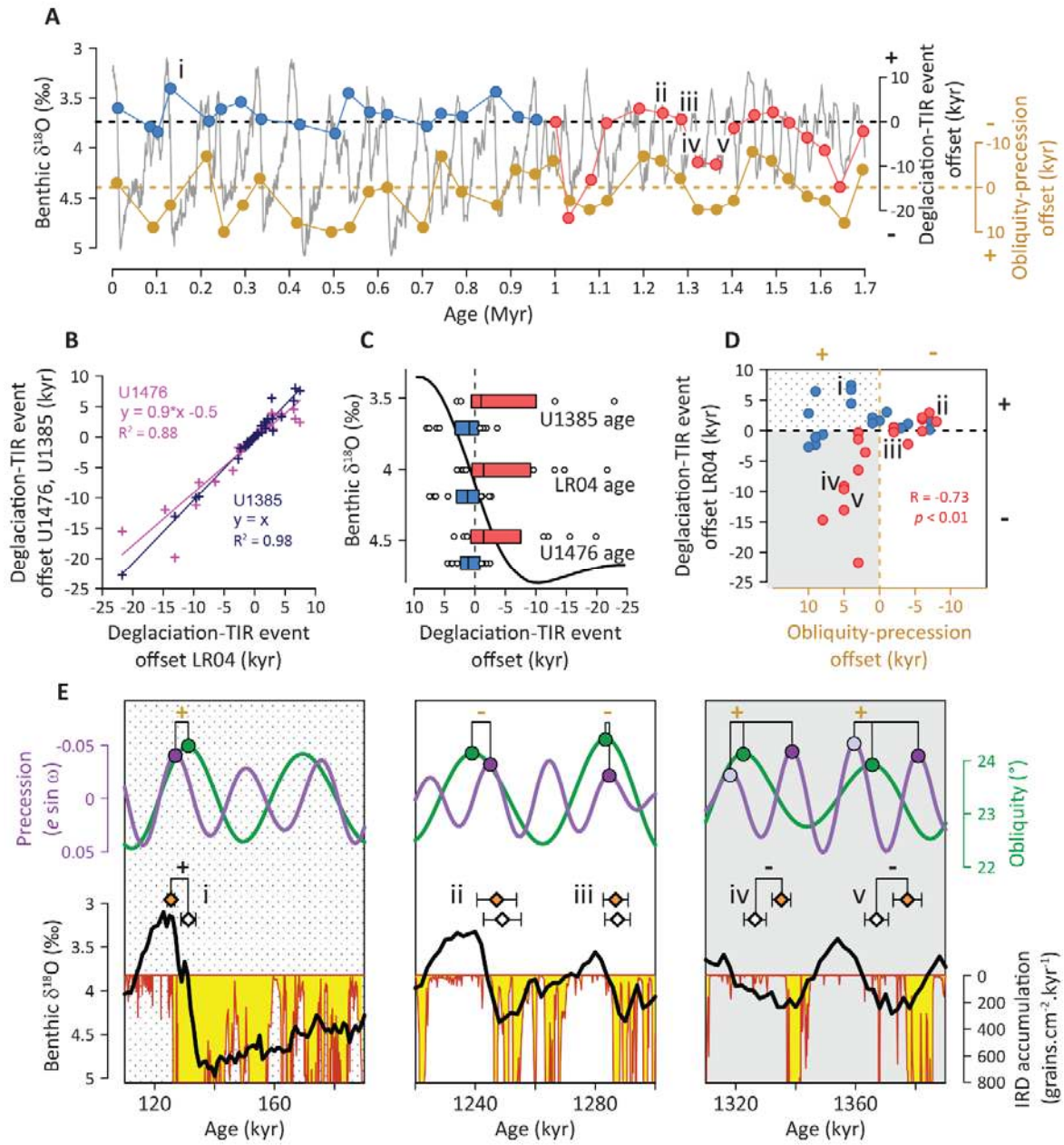
Figure 6. Changing orbits control the relative timing of terminal ice rafting versus deglaciation. (A)

Offsets between the end of TIR events and deglacial transitions as a function of benthic δ^{18}O (blue and

red circles; a zero offset means that the end of TIR occurs in parallel with the mid-point of deglaciation -

defined as the maximum rate of change in δ^{18}O (*13*)- while a negative offset indicates that TIR ends

earlier than the mid-point) compared with offsets between maxima in obliquity and their nearest minima in precession (gold circles; negative offset indicates that the closest precession peak occurs before the peak in obliquity and vice versa). (B) Comparison of the 3 age models for calculating offsets. (C) Box plots representing the calculated offsets before (red) and after (blue) 1Ma. Black curve is the smoothed LR04 stack across Termination 2 for context. (D) Calculated offsets before (red) and after (blue) 1Ma versus the phasing between obliquity and precession (Roman numerals refer to part (A)). For events >1Ma the relationship is significant (p<0.005, R=-0.73) (*13*). (E) Examples of the various phasing between obliquity and precession shown in (D) and associated offsets between TIR events and deglaciation. Orange diamonds represent the end of TIR events, white diamonds are deglacial transitions (each data point represents the mean of the 3 age model results ±1σ).

1
2
3
4
5

Supplementary Materials for

6

Persistent influence of precession on northern ice sheet variability since the early Pleistocene

9

Stephen Barker, Aidan Starr, Jeroen van der Lubbe, Alice Doughty, Gregor Knorr, Stephen Conn, Sian Lordsmith, Lindsey Owen, Alexandra Nederbragt, Sidney Hemming, Ian Hall, Leah Levay and the IODP Exp 361 Shipboard Scientific Party

Correspondence to: barkers3@cf.ac.uk

15
16

This PDF file includes:

18

IODP Exp 361 Shipboard Scientific Party information
Materials and Methods
Supplementary References (*27-50*)
Figs. S1 to S17
Tables S1 to S2
Caption for Data S1

25
26
27
28

29   **IODP Exp 361 Shipboard Scientific Party information**

30

31   Hall, I.R.[1], Hemming, S.R.[2], LeVay, L.J.[3], Barker, S.[1], Berke, M.A.[4], Brentegani, L.[5], Caley, T.[6],
32   Cartagena-Sierra, A.[4], Charles, C.D.[7], Coenen, J.J.[8], Crespin, J.G.[6], Franzese, A.M.[9], Gruetzner,
33   J.[10], Han, X.[11], Hines, S.K.V.[12], Jimenez Espejo, F.J.[13], Just, J.[14], Koutsodendris, A.[15], Kubota,
34   K.[16], Lathika, N.[17], Norris, R.D.[7], Periera dos Santos, T.[18], Robinson, R.[19], Rolison, J.M.[20],
35   Simon, M.H.[21], Tangunan, D.[1], van der Lubbe, H.J.L.[22], Yamane, M.[23], and Zhang, H[24].

36

37   [1]School of Earth and Environmental Sciences, Cardiff University, UK. [2]Lamont-Doherty Earth
38   Observatory, Columbia University, USA. [3]International Ocean Discovery Program, Texas A&M
39   University, USA. [4]Department of Civil Engineering & Geological Sciences, University of Notre
40   Dame, USA. [5]Earth and Environmental Sciences, University of Technology Queensland,
41   Australia. [6]EPOC, UMR CNRS 5805, University of Bordeaux, France. [7]Scripps Institution of
42   Oceanography, University of California, USA. [8]Department of Geology, Northern Illinois
43   University, USA. [9]School of Earth and Environmental Sciences, Hostos Community College
44   (CUNY), USA. [10]Geosciences, Alfred-Wegener-Institut for Polar and Marine Research,
45   Germany. [11]Second Institute of Oceanography, Key Laboratory of Submarine Science, China.
46   [12]Woods Hole Oceanographic Institution, Woods Hole, USA. [13]Institute of Biogeosciences,
47   Japan Agency for Marine-Earth Science and Technology (JAMSTEC), Japan. [14]Geologisches
48   Institut, Universität Kõln, Germany. [15]Institute of Earth Sciences, University of Heidelberg,
49   Germany. [16]Atmosphere and Ocean Research Institute, University of Tokyo, Japan. [17]National
50   Centre for Polar and Ocean Research, Ministry of Earth Sciences, Goa, India. [18]Institute for
51   Geosciences, Universidade Federal Fluminense (UFF), Brazil. [19]Graduate School of
52   Oceanography, University of Rhode Island, USA. [20]Lawrence Livermore National Laboratory,
53   USA. [21]NORCE, Bergen, Norway. [22]Department of Earth Sciences, Vrije Universiteit
54   Amsterdam, Netherlands. [23]Institute for Space-Earth Environmental Research, Nagoya
55   University, Japan. [24]School of Ecology and Environmental Science, Yunnan University, China

56

57   **Materials and Methods**

58

59   <u>Sample preparation</u>

60   For this study we processed 1,857 samples along the splice of ODP 983 (*27*) and 2,366
61   samples along the splice of IODP U1476 (*28*) (Fig. S1). Sediment samples were spun overnight
62   and washed with DI water through a 63μm sieve before being dried at 40°C. IRD counts from
63   Site 983 were made on the >150μm fraction after splitting to yield approximately 300 entities
64   following previous studies (*10, 29, 30*). IRD was considered as the total number of
65   lithogenic/terrigenous grains counted. Benthic foraminiferal stable isotopes from Site U1476
66   were performed on *Cibicidoides wuellerstorfi* (ideally 3 individuals) picked from the 250-355μm
67   fraction (occasionally >355μm) and measured at Cardiff University using a Thermo Finnigan
68   MAT 253 mass spectrometer linked online to a Carbo Kiel carbonate preparation device. Long-
69   term precision is ±0.05‰ for $\delta^{18}O$ and ±0.021‰ for $\delta^{13}C$ (±1σ). Results are calibrated to an
70   internal laboratory standard (BCT63) and presented relative to the Vienna Pee Dee Belemnite
71   scale. The records from U1476 presented here have an average temporal resolution of 840 years

72 and span the interval ~1.8Ma to present. A lower resolution subset of the δ^{18}O dataset (every 4th
73 sample) was presented recently by van der Lubbe *et al.* (*31*).
74
75 <u>Age model development</u>
76   ODP Site 983 is part of the LR04 benthic δ^{18}O stack (*14*) and we are therefore able to use
77 its corresponding (LR04) age model as one of our timescales (Fig. S2c). We also developed an
78 'LR04' age model for Site U1476 by tuning its record of benthic δ^{18}O to LR04 (Fig. S2b). We
79 used a limited number of tie points (34 over the last 1.7Myr) to avoid over-tuning, which we
80 suggest provides a more objective approach when testing for the presence of orbital frequencies.
81 Even with this limited number of tuning points we observe an excellent correlation between our
82 new benthic δ^{18}O record and LR04 (δ^{18}O$_{U1476}$+0.64 = 1.003*δ^{18}O$_{LR04}$ R^2=0.998), which implies
83 that the site of U1476 reflects reasonably well the global 'average' ocean composition, at least
84 with respect to δ^{18}O.
85
86   Next we develop an absolute age model for ODP 983 based on the growing body of
87 ^{40}Ar$^{/39}$Ar-dated magnetic polarity reversals and magnetic excursions (*15, 32*):
88
89   Step (1): ODP Site 983 has excellent records of relative geomagnetic paleointensity (it is
90 part of the PISO-1500 stack (*33*)) and inclination (*27, 34, 35*) (Fig. S2e, f), which makes it an
91 ideal candidate for developing an absolute age scale through this approach. We therefore use a
92 recent compilation (*15*) of ^{40}Ar$^{/39}$Ar dates from volcanic sequences to assign absolute ages to
93 ODP 983 (Table S1). In order to standardize the assignment of ages we identify minima in
94 paleomagnetic intensity (as described by Channell *et al.* (*15*) and depicted in their Figs. 1, 4, 5,
95 8) and/or transitions in inclination at Site ODP983 associated with ^{40}Ar$^{/39}$Ar dated horizons (*15*).
96 Symmetrical depth uncertainties are calculated as the width of the corresponding minima
97 (intensity) or transition (inclination). An initial absolute age model for ODP 983 (pMag) was
98 constructed by linear interpolation between these points and is illustrated in Figure S2e-g.
99
100   Step (2): Sediment accumulation rates at ODP Site 983 are sensitive to the overflows of
101 deep water crossing the Iceland-Scotland Ridge (*10*) and are highly variable (Fig. S2k).
102 Sedimentation rates at Site U1476 are less variable (Fig. S2j) due to its location away from major
103 bottom currents. However, the shipboard paleomagnetic data obtained for U1476 were heavily
104 overprinted (*36, 37*) and could not be used to develop an absolute paleomagnetic timescale
105 directly. We therefore transfer the Ar/Ar ages from Site 983 (Table S1) to the U1476 depth scale
106 by graphically aligning the benthic δ^{18}O records of both sites. To correlate two signals in this
107 manner, it is preferable to identify intervals of high rate of change (i.e. transitions in the δ^{18}O
108 record), however the Ar/Ar ages assigned to ODP983 do not always align with recognizable
109 transitions in the δ^{18}O record (Fig. S2g, h). Therefore, we chose to align the nearest recognizable
110 δ^{18}O transitions preceding and succeeding each Ar/Ar age with the corresponding transitions in
111 U1476, before using linear interpolation to transfer the age onto the U1476 depth scale. We then
112 take the distance from this point to the nearest transition as the 3 sigma U1476 depth uncertainty
113 for this point; assuming that the Ar/Ar age must fall between the two transitions. The result of
114 this step is a set of Ar/Ar ages (with uncertainties) and the corresponding depths in U1476, also
115 with uncertainties (Table S1).
116

117   Step (3): Next, we input the U1476 age-depth tie points from step 2 into the deterministic
118 age-depth modelling software "Undatable" (*38*) using an "x-factor" of 0.5 and 10^5 iterations.
119 To ensure that the paleomagnetic tie points are constrained we do not include them in the
120 bootstrapping routine. The result is the "U1476pMag" age model for U1476 with age uncertainty
121 estimates (Figs. S2, S3). As shown in Fig. S3a, c, the uncertainty estimates for the U1476pMag
122 age model are typically large (mean ~16kyr 1σ), increasing up to 40kyr at ~1.5Ma where age
123 control points are particularly sparse. On the other hand the offset between our absolute
124 (U1476pMag) age model for U1476 and that derived by tuning to LR04 is generally much
125 smaller than the age uncertainty estimates for U1476pMag, averaging 6.6kyr (in absolute terms)
126 over the last 1.8Myr (Fig. S3b, d). We suggest that our final U1476pMag age model with its
127 corresponding record of benthic δ^{18}O (Fig. S2h) might become a standard absolute reference
128 timescale (spanning the last ~1.8Myr) for future studies.
129
130   Step (4): Finally, the absolute age model U1476pMag was transferred back to ODP 983 by
131 further tuning between their records of benthic δ^{18}O (Fig. S2i). Note that the final absolute age
132 model for ODP Site 983 (U1476pMag) includes the initial constraints obtained in step (1) above.
133
134   A third age model for ODP Site 983 was constructed by tuning to the reference timescale
135 published for IODP Site U1385 (*16*). Following our previous study (*12*) we tuned our records
136 from ODP Site 983 to the U1385 record of log Ca/Ti acquired by XRF scanning (*16*) (Fig. S4).
137 At the site of U1385 log(Ca/Ti) is thought to reflect changes in the relative supply of biogenic
138 carbonate and detrital sediment. Biogenic carbonate apparently increases during interglacial and
139 interstadial periods and decreases during glacial and stadial periods and therefore provides a
140 proxy for high northern latitude millennial-scale climate variability. For the interval 1.2-1.7Ma
141 we limited our tuning to features in the IRD and coarse fraction records. Details for the interval
142 0-1.2Ma were reported previously (*12*). Hodell et al. (*16*) derived several age models for U1385
143 but here we employ that obtained by correlating peaks in L* (i.e. sediment colour) to local
144 summer insolation at 37°N, based on the observation of a strong precession-like signal within L*
145 that displays similar amplitude modulation as precession (a function of eccentricity).
146
147   The final timeseries of IRD accumulation and IRD grains per gram versus core depth are
148 shown in Figure S5.
149
150 <u>IRD accumulation rates</u>
151   IRD accumulation rates were calculated from IRD/g and dry bulk accumulation rates,
152 obtained by combining linear sedimentation rates with an estimate for dry bulk density. Dry bulk
153 density was derived from continuous GRAPE density measurements calibrated with discrete
154 (index property) measurements of wet and dry bulk density (*27*) according to equation (1):
155
156 Dry Bulk Density = (GRAPE+0.17)*1.5547-1.5719   (1)
157
158 <u>Linear IRD versus log IRD</u>
159   In general the largest peaks in IRD accumulation are associated with deglacial intervals
160 (Fig. S6). This is most apparent when IRD is plotted on a linear scale and results in an apparent
161 time lag (on G-IG timescales) between LR04 (*14*) and IRD accumulation (which is plotted here
162 on its LR04 age model). However, no lag is observed between the LR04 stack and log IRD (Fig.

163   S6). This is because taking the log of IRD accumulation (+1) enhances variability when IRD
164   accumulation is low to moderate, which we argue highlights the fact that ice rafting occurs
165   (albeit at relatively low levels) whenever ice sheets are large enough to experience marine
166   calving. By extension it follows that our record of log IRD accumulation reflects the growth
167   (extension) and decay (retraction) of circum-NE Atlantic ice sheets relatively closely (compared
168   to linear IRD) and that this growth and decay in turn mirrors (at low frequencies) variations in
169   the LR04 stack. The corollary of this is that in general the LR04 stack mirrors variations in
170   northern ice sheet variability.

171

172   <u>Algorithm to determine the start end of significant ice rafting</u>
173   We wish to assess the timing of ice rafting events with respect to orbital parameters and
174   changing sea level (in this case the LR04 stack). Initially, interglacial (IG) events are identified
175   by picking minima in the LR04 benthic $\delta^{18}O$ record after applying a 10kyr smooth, which
176   minimizes the number of un-named warm stages while preserving most of the named interglacial
177   stages (*39*) (Fig. S7). We also impose a maximum absolute value of 4.25‰ to avoid picking
178   minima during glacial intervals. Deglacial transitions in LR04 are identified as minima in the
179   smoothed first time-differential of the smoothed record of LR04 (Fig. S8).

180

181   To assess the start and end of significant ice rafting in the IRD record from ODP 983 we
182   develop an 'IRD index' which discriminates between intervals of high and low IRD
183   accumulation. We first apply a 13-point running mean (implemented via filtfilt in Matlab i.e. run
184   forwards and backwards) to the record of log IRD before detrending to account for the generally
185   higher concentrations of IRD in more recent sediments (by subtraction of a linear ramp from 0 to
186   0.5 over the 1.7Myr record; Fig. S9). Our next step is to choose a threshold above which we
187   consider ice rafting significant. We find that a value of log IRD = 1.3 (equivalent to 20grains.cm^{-}
188   ^{2}.kyr^{-1}) is successful at delineating between relatively icy versus ice-free conditions throughout
189   the whole 1.7Myr record (Fig. S8, S9). Each sample interval is then assigned a value
190   representing either high or low IRD to generate the IRD index (Fig. S8, S9).

191

192   To identify the onset of significant ice rafting the algorithm searches for the first transition
193   to high IRD following each interglacial. A similar procedure is used to identify the end of ice
194   rafting prior each interglacial, with the additional constraint that the preceding interval of high
195   IRD must be at least 2.8kyr in duration. This is because we are interested in the major IRD
196   events associated with glacial terminations in the late Pleistocene (here termed TIR events).
197   Temporal offsets between the onset and end of (terminal) ice rafting versus minima and maxima
198   in obliquity and precession (Fig. 5) are then obtained by identifying the nearest orbital peak to
199   each event of interest and differencing their respective ages. The algorithm was optimized (see
200   below) using the LR04 age model and ages for each transition in IRD were transferred to the
201   other age models via their respective depth in core. Note though that the closest orbital peaks in
202   each case are allocated independently i.e. a different peak might be assigned for the same
203   transition in IRD depending on the age model employed.

204

205   The observed relationship between the end of a TIR event and deglaciation versus the
206   obliquity-precession offset for events >1Ma, as shown in Fig. 6D, was assessed using the
207   surrogateCor function in Astrochron (*22*) and is found to be significant: R= -0.73, p<0.005
208   (based on 2000 phase-randomized surrogate series in the Monte Carlo simulation).

209
210   In Figure S10 we show an analysis to demonstrate the sensitivity of the algorithm to the
211   various parameter values assigned (using the LR04 age model). Our parameter choices were
212   made in order to maximize the number of TIR events identified where possible. As can be seen,
213   the main conclusions of our study are insensitive to a wide range of parameter values. The
214   parameter with the most substantial influence on the results is the threshold used to discriminate
215   between low and high IRD levels. Use of a very low threshold (e.g. 0.5) means that the end of a
216   TIR event will necessarily occur relatively close to the respective IG event irrespective of when
217   the major episode of deglacial ice rafting ends (as discriminated by eye) because a certain
218   amount of ice rafting continues during the early stages of most interglacials. Since the LR04 age
219   model is orbitally tuned, this results in a rather monotonous temporal relationship observed
220   between the end of TIR events (according to the algorithm with low threshold) and the phase of
221   obliquity and precession. Use of a low threshold also reduces the number of TIR events
222   identified in the <1Ma portion of the record because of the generally higher fluxes of IRD at
223   these times (a TIR event cannot be detected if ice rafting continues throughout the associated
224   IG).
225
226   Temporal offsets between deglaciations and maxima in obliquity are obtained by
227   identifying the closest obliquity peaks to each deglacial transition and differencing (Fig. S11).
228   Since the record of benthic δ^{18}O from ODP Site 983 is part of the LR04 stack (*14*), we can
229   transfer the ages of deglacial transitions in LR04 onto the other age models developed for ODP
230   Site 983. This is done by transferring the age of each deglacial transition in the LR04 stack into
231   the depth domain of 983 using the LR04 age model published by ref (*14*). Each depth is then
232   assigned ages on the U1476pmag or U1385 age models described above. Figure S11 reveals the
233   close correspondence observed between deglaciations and rising to maximum obliquity
234   throughout the last 1.7Myr for all three age models employed here.
235
236
237   <u>Circular statistics</u>
238   Circular statistics shown in Figs. 5 and S11 were calculated using the CircStat toolbox for
239   MATLAB developed by Berens (*40*). Below we summarize the various functions employed
240   here:
241
242   **Rayleigh test** for a unimodal deviation from uniformity tests the null hypothesis (*H₀*) that the
243   population is distributed uniformly around the circle. The approximate p-value under *H₀* is
244   computed as:
245

$$p = exp\left[\sqrt{(1 + 4N + 4(N^2 - R_n^2))} - (1 + 2N)\right]$$

247
248   where $R_n = R \cdot N$ (see below for definition of R). The lower the value of p, the greater the
249   likelihood that *H₀* can be rejected.
250
251   **Mean angle** (ᾱ). Individual directions are first transformed to unit vectors in the 2-D plane:
252

$$r_i = \begin{pmatrix} \cos \alpha_i \\ \sin \alpha_i \end{pmatrix}$$

254

255   The vectors r_i are then vector averaged:

256     $$\bar{r} = \frac{1}{N} \sum_i r_i$$

257   where $\bar{r}$ is the mean resultant vector. To yield the mean angular direction $\bar{\alpha}$, $\bar{r}$ is transformed
258   using the four quadrant inverse tangent function (*40*).

259

260   **Resultant vector length** (R):

261

262     $$R = ||\bar{r}||$$

263

264   R varies between 0 and 1 with R closer to 1 if the data are more concentrated around the mean
265   direction.

266

267   **Confidence Intervals for the Mean Direction.** The $(1-\delta)$%-confidence intervals for the

268   population mean are computed for $R \leq 0.9$ and $R > \sqrt{\chi^2_{\delta,1}/2N}$ using:

269

270     $$d = \arccos\left[\frac{\sqrt{\dfrac{2N\left(2R_n^2 - N\chi^2_{\delta,1}\right)}{4N - \chi^2_{\delta,1}}}}{R_n} \right]$$

271

272   where $R_n = R \cdot N$ and for $R > 0.9$ using:

273

274     $$d = \arccos\left[\frac{\sqrt{N - (N^2 - R_n^2)\exp\left(\chi^2_{\delta,1}/N\right)}}{R_n} \right]$$

275

276   In both cases, the lower confidence limit of the mean, $L_1 = \bar{\alpha} - d$ and the upper confidence limit,
277     $L_2 = \bar{\alpha} + d$.

278

279   In order to benefit from the use of multiple age models we combine the results from the 3
280   age models as follows: Firstly, because the LR04 and U1385 age models are both based on
281   orbital tuning, they are not truly independent. We therefore take the mean age for each IRD
282   transition using these 2 age models before applying the algorithm to search for the nearest orbital
283   peaks. We then combine these results with those from the U1476pmag age model before
284   implementing CircStat. By this combination we are weighting orbital and non-orbital age
285   modelling methods equally.

286

287

288

289   Frequency analysis

290   All frequency analyses were performed on evenly resampled (200yr for logIRD and 1kyr
291   for the LR04 stack and the benthic δ^{18}O record from U1476) timeseries. Bandpass filtering was
292   performed using a Taner filter (roll-off rate = 10^4) within the Astrochron (*22*) Package for R
293   (*41*). For spectral analyses we employed the 'robust' (multi-taper spectral analysis with median
294   smoothing of the spectrum to estimate the underlying noise background) AR(1) method of (*17*)
295   (updated by (*18*)) and an alternative spectral noise estimation method (LOWSPEC (*18*)) which is
296   designed to overcome some of the problems associated with the AR1 method (including inflated
297   confidence level estimates and excessive clumping of false positives within the low frequency
298   portion of the spectrum). LOWSPEC simultaneously allows for departures from the AR(1)
299   assumption, and is more able to accurately identify astronomical signals when they are present in
300   the data (*18*). The power spectra and estimated red noise models for each analysis are shown in
301   Fig. S12-14.

302

303   We also apply an MTM Harmonic F-test, designed to test for phase-coherent sinusoids in
304   white or colored noise (*18, 42, 43*) and which is quasi-independent of the other tests we apply.
305   Following the procedure outlined by (*18*) and implemented in the Astrochron package for R (*22*),
306   an F-test peak is reported if it achieves the specified MTM harmonic confidence level (>90%)
307   while also achieving the specified robust red noise or LOWSPEC confidence level ± half the
308   power spectrum bandwidth resolution. In addition, significant F-tests must occur on a local
309   power spectrum high, which is parameterized as occurring above the local LOWSPEC or robust
310   red noise background estimate. We note that although the F-test confidence is relatively high for
311   peaks within the precession band of the 1250-1700ka interval of logIRD record (Fig. S15), none
312   of these peaks pass the test criteria outlined above.

313

314   Wavelet transforms and cross wavelet transforms (Figs. S16, S17) were produced using the
315   Matlab functions presented by Grinsted and Moore (*44*), implemented on evenly resampled
316   (200yr for logIRD and 1kyr for the LR04 stack and δ^{18}O from U1476; 1kyr resampling was used
317   for both logIRD and LR04 in the cross wavelet transform) timeseries. Note that the significance
318   level within cross wavelet transform may be overestimated as a result of strong power within
319   either of the individual wavelets (*45*).

320

321   Insolation metrics

322   Calculations for determining the insolation metrics shown in Figure 1 were based on the
323   Palinsol (*46*) package for R, using the astronomical solutions of Laskar (*47*).

324

325   **Supplementary References**

326

327   27.   E. Jansen, M. E. Raymo, P. Blum, *Proceedings of the Ocean Drilling Program, Initial Reports. Vol.*
328   *162*. (Texas A & M University, Ocean Drilling Program, 1996).
329   28.   I. Hall, S. Hemming, L. LeVay, S. Barker, M. Berke, L. Brentegani, T. Caley, A. Cartagena-Sierra, C.
330   Charles, J. Coenen, in *Proceedings of the International Ocean Discovery Program, 361*.
331   (International Ocean Discovery Program, 2017).
332   29.   G. Bond, H. Heinrich, W. Broecker, L. Labeyrie, J. McManus, J. Andrews, S. Huon, R. Jantschik, S.
333   Clasen, C. Simet, K. Tedesco, M. Klas, G. Bonani, S. Ivy, Evidence for massive discharges of

334   icebergs into the north Atlantic Ocean during the Last Glacial Period. *Nature* **360**, 245-249
335   (1992).

336   30.   G. C. Bond, R. Lotti, Iceberg Discharges into the North-Atlantic on Millennial Time Scales During
337   the Last Glaciation. *Science* **267**, 1005-1010 (1995).

338   31.   H. J. L. v. d. Lubbe, I. R. Hall, S. Barker, S. R. Hemming, J. Just, T. F. Baars, A. Starr, J. C. A.
339   Joordens, Shipboard_scientists, Invigoration of Indian Ocean zonal circulation drove Pleistocene
340   eastern Africa aridification in review (2021).

341   32.   B. S. Singer, A Quaternary geomagnetic instability time scale. *Quaternary Geochronology* **21**, 29-
342   52 (2014).

343   33.   J. Channell, C. Xuan, D. Hodell, Stacking paleointensity and oxygen isotope data for the last 1.5
344   Myr (PISO-1500). *Earth and Planetary Science Letters* **283**, 14-23 (2009).

345   34.   J. E. T. Channell, D. A. Hodell, B. Lehman, Relative geomagnetic paleointensity and delta O-18 at
346   ODP Site 983 (Gardar Drift, North Atlantic) since 350 ka. *Earth and Planetary Science Letters* **153**,
347   103-118 (1997).

348   35.   J. E. T. Channell, H. F. Kleiven, Geomagnetic palaeointensities and astrochronological ages for
349   the Matuyama-Brunhes boundary and the boundaries of the Jaramillo Subchron:
350   palaeomagnetic and oxygen isotope records from ODP Site 983. *Philosophical Transactions of*
351   *the Royal Society of London Series a-Mathematical Physical and Engineering Sciences* **358**, 1027-
352   1047 (2000).

353   36.   I. R. Hall, S. R. Hemming, L. J. LeVay, S. R. Barker, M. A. Berke, L. Brentegani, T. Caley, A.
354   Cartagena-Sierra, C. D. Charles, J. J. Coenen, Proceedings of the International Ocean Discovery
355   Program; South African climates (Agulhas LGM density profile); Expedition 361 of the riserless
356   drilling platform, Port Louis, Mauritius, to Cape Town, South Africa; Sites U1474-U1479, 30
357   January-31 March 2016. (2017).

358   37.   H. J. L. van der Lubbe, I. R. Hall, S. Barker, S. R. Hemming, T. F. Baars, A. Starr, J. Just, B. C.
359   Backeberg, J. C. A. Joordens, Indo-Pacific Walker circulation drove Pleistocene African
360   aridification. *Nature* **598**, 618-623 (2021).

361   38.   B. C. Lougheed, S. Obrochta, A Rapid, Deterministic age-depth modeling routine for geological
362   sequences with inherent depth uncertainty. *Paleoceanography and Paleoclimatology* **34**, 122-
363   133 (2019).

364   39.   L. B. Railsback, P. L. Gibbard, M. J. Head, N. R. G. Voarintsoa, S. Toucanne, An optimized scheme
365   of lettered marine isotope substages for the last 1.0 million years, and the climatostratigraphic
366   nature of isotope stages and substages. *Quaternary Science Reviews* **111**, 94-106 (2015).

367   40.   P. Berens, CircStat: a MATLAB toolbox for circular statistics. *J Stat Softw* **31**, 1-21 (2009).

368   41.   R_Core_Team, R: A Language and Environment for Statistical Computing. *R Foundation for*
369   *Statistical Computing* **Vienna, Austria**, https://www.R-project.org/ (2020).

370   42.   D. J. Thomson, Spectrum estimation and harmonic analysis. *Proceedings of the IEEE* **70**, 1055-
371   1096 (1982).

372   43.   D. B. Percival, A. T. Walden, *Spectral analysis for physical applications*. (cambridge university
373   press, 1993).

374   44.   A. Grinsted, J. C. Moore, S. Jevrejeva, Application of the cross wavelet transform and wavelet
375   coherence to geophysical time series. *Nonlinear processes in geophysics* **11**, 561-566 (2004).

376   45.   D. Maraun, J. Kurths, Cross wavelet analysis: significance testing and pitfalls. *Nonlinear Processes*
377   *in Geophysics* **11**, 505-514 (2004).

378   46.   M. Crucifix, Palinsol: insolation for palaeoclimate studies, R package version 0.93.
379   https://bitbucket.org/mcrucifix/insol (2016).

380 47. J. Laskar, P. Robutel, F. Joutel, M. Gastineau, A. C. M. Correia, B. Levrard, A long-term numerical
381   solution for the insolation quantities of the Earth. *Astronomy & Astrophysics* **428**, 261-285
382   (2004).
383 48. R. A. Locarnini, A. V. Mishonov, J. I. Antonov, T. P. Boyer, H. E. Garcia, O. K. Baranova, M. M.
384   Zweng, D. R. Johnson, in *NOAA Atlas NESDIS 68,* S. Levitus, Ed. (U.S. Government Printing Office,
385   Washington, D.C., 2010), pp. 184.
386 49. M. E. Raymo, D. W. Oppo, B. P. Flower, D. A. Hodell, J. F. McManus, K. A. Venz, K. F. Kleiven, K.
387   McIntyre, Stability of North Atlantic water masses in face of pronounced climate variability
388   during the Pleistocene. *Paleoceanography* **19**, PA2008, doi:10.1029/2003PA000921 (2004).
389 50. H. F. Kleiven, I. R. Hall, I. N. McCave, G. Knorr, E. Jansen, Coupled deep-water flow and climate
390   variability in the middle Pleistocene North Atlantic. *Geology* **39**, 343-346 (2011).

391

392
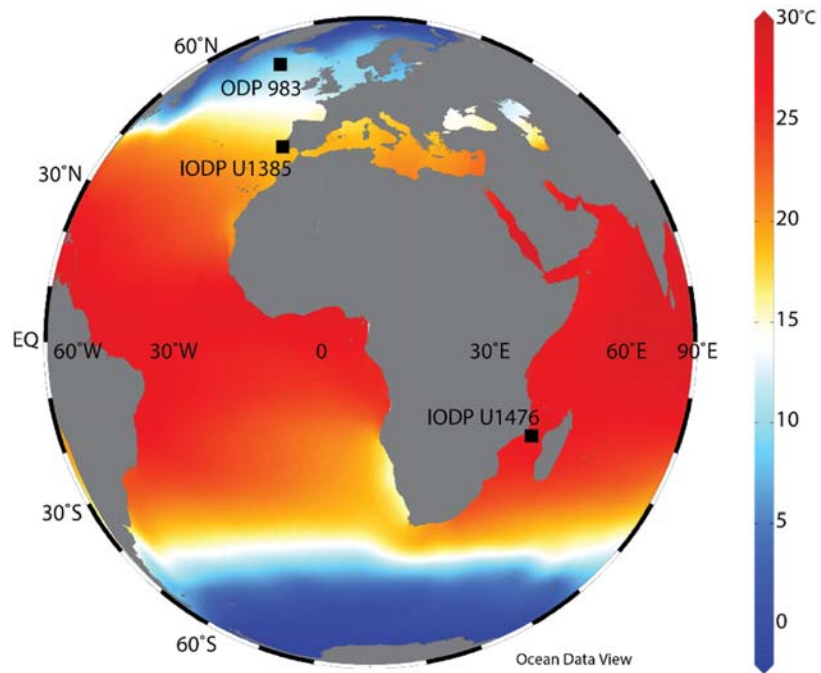
393

394 **Fig. S1.**
395 Locations of Sites 983, U1385 and U1476 plotted with annual sea surface temperature (*48*).
396
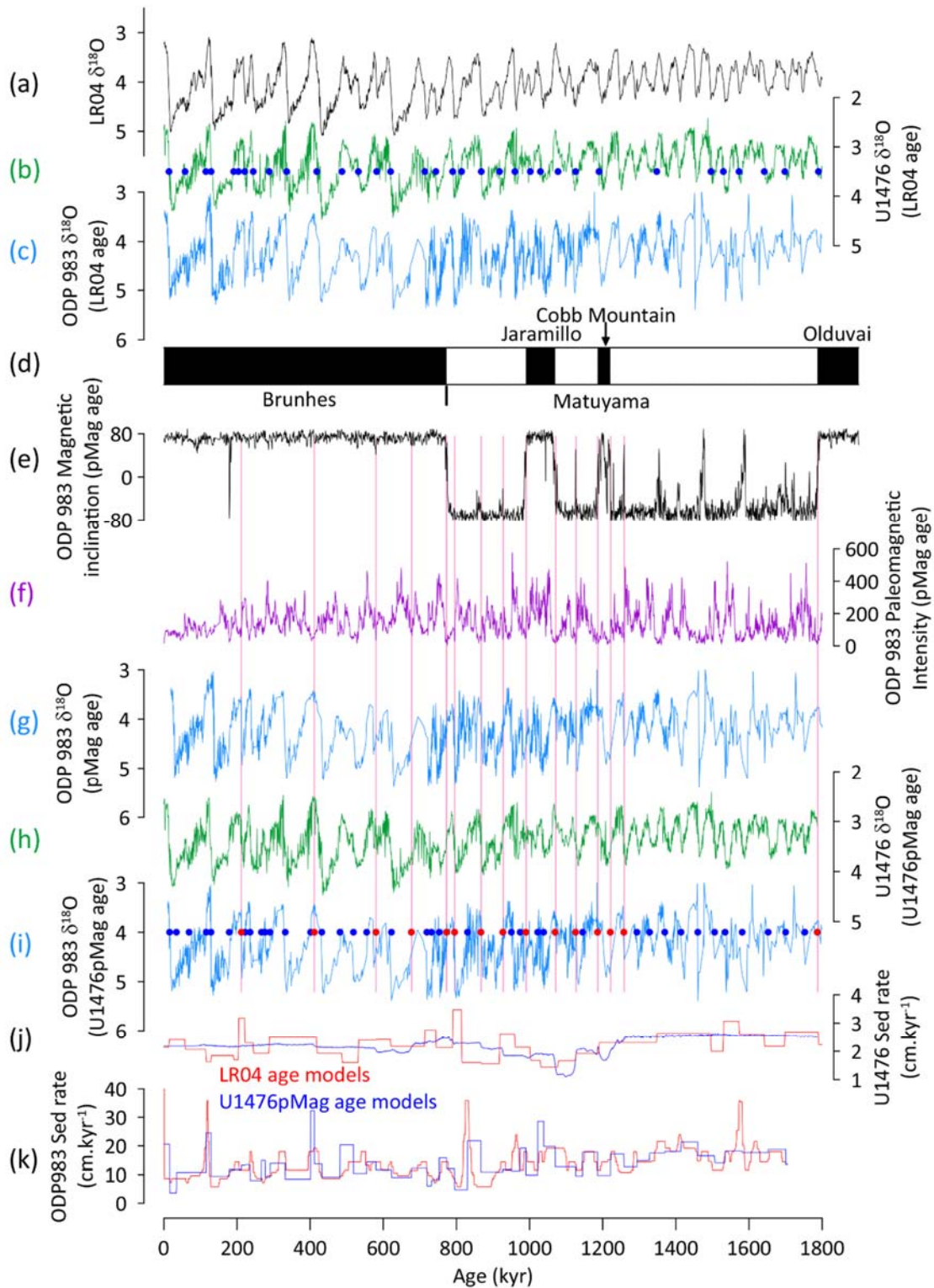
Fig. S2.

Development of absolute timescales for ODP 983 and U1476 and LR04 timescale for U1476. (a)
The LR04 stack (*14*) was used as a tuning target for the benthic δ¹⁸O record of U1476 to derive

400   the LR04 age model for this site (b; blue circles are tuning points). (c) We use the published

401   LR04 age model for ODP Site 983 as one of our timescales. (d) Major paleomagnetic chrons,

402   sub-chrons and excursions of the past 1.8Myr. Records of magnetic inclination (e) and

403   paleomagnetic intensity (f) from ODP 983 (*27, 34, 35*) on the initial (pMag) absolute timescale

404   derived from Table S1 (vertical red lines are absolute age constraints). (g) the benthic δ^{18}O

405   record from ODP 983 (*34, 49, 50*) on its initial absolute age model (pMag) is used to transfer

406   absolute constraints onto U1476 to derive the final absolute timescale, U1476pMag. (h) the

407   benthic δ^{18}O record from U1476 (U1476pMag age) is then used as a tuning target for ODP 983

408   to derive the U1476pMag age model for this site (i). Blue circles in part (i) are additional

409   constraints from tuning to U1476 benthic δ^{18}O on the U1476pMag timescale. (j, k)

410   sedimentation rates for the 2 sites on their LR04 and U1476pMag age models.

411
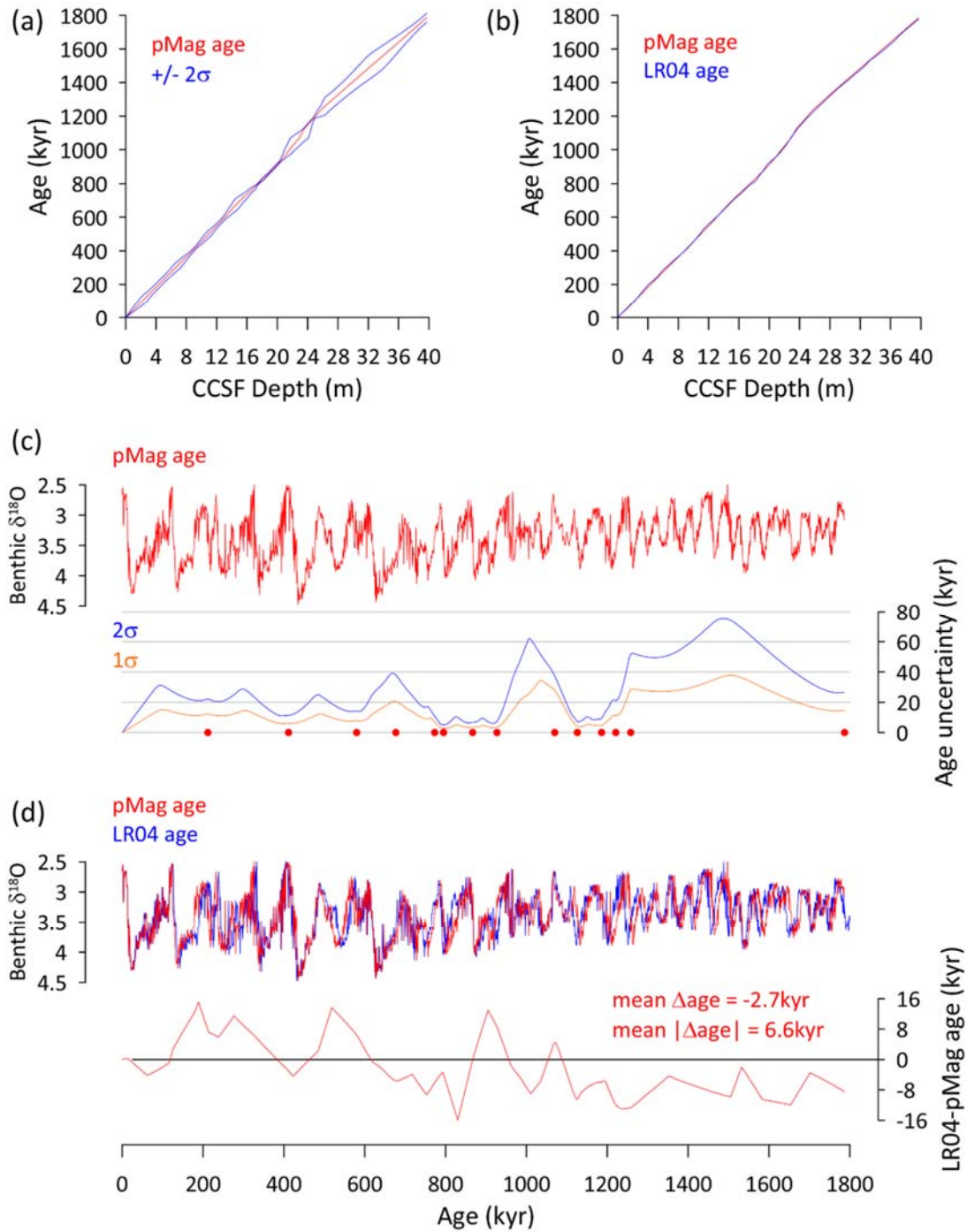
412
413 **Fig. S3**.
414 U1476pMag versus LR04 age models for U1476. (a) U1476pMag age vs depth with ±2σ plotted.
415 (b) U1476pMag and LR04 age vs depth. (c) Benthic δ¹⁸O from U1476 plotted on its U1476pMag
416 age model with age uncertainties versus time (red circles are age control points; Table S1). (d)
417 Benthic δ¹⁸O from U1476 on its U1476pMag and LR04 age models with the age offset plotted
418 versus time.

419

420
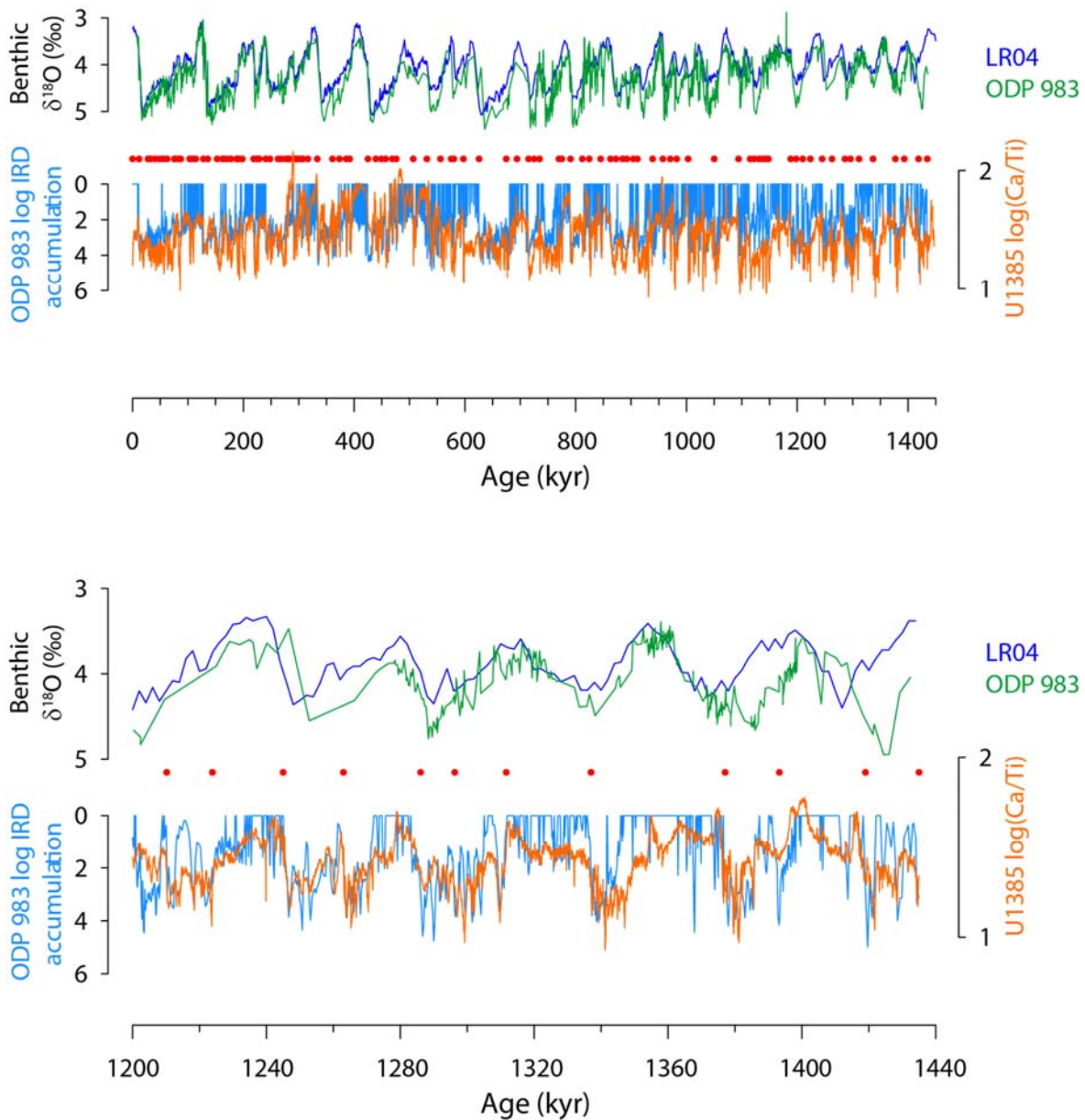
Fig. S4.

Construction of the U1385 age model for ODP Site 983. Upper panel shows whole record (the U1385 age scale (*16*) does not extend beyond 1450ka). Lower panel shows the portion developed here (earlier portion was presented previously (*12*)). In both panels the benthic δ¹⁸O record from ODP 983 (*34, 49, 50*) is plotted on the U1385 age model and compared with the LR04 stack on its own timescale. Red circles are tuning points.

427
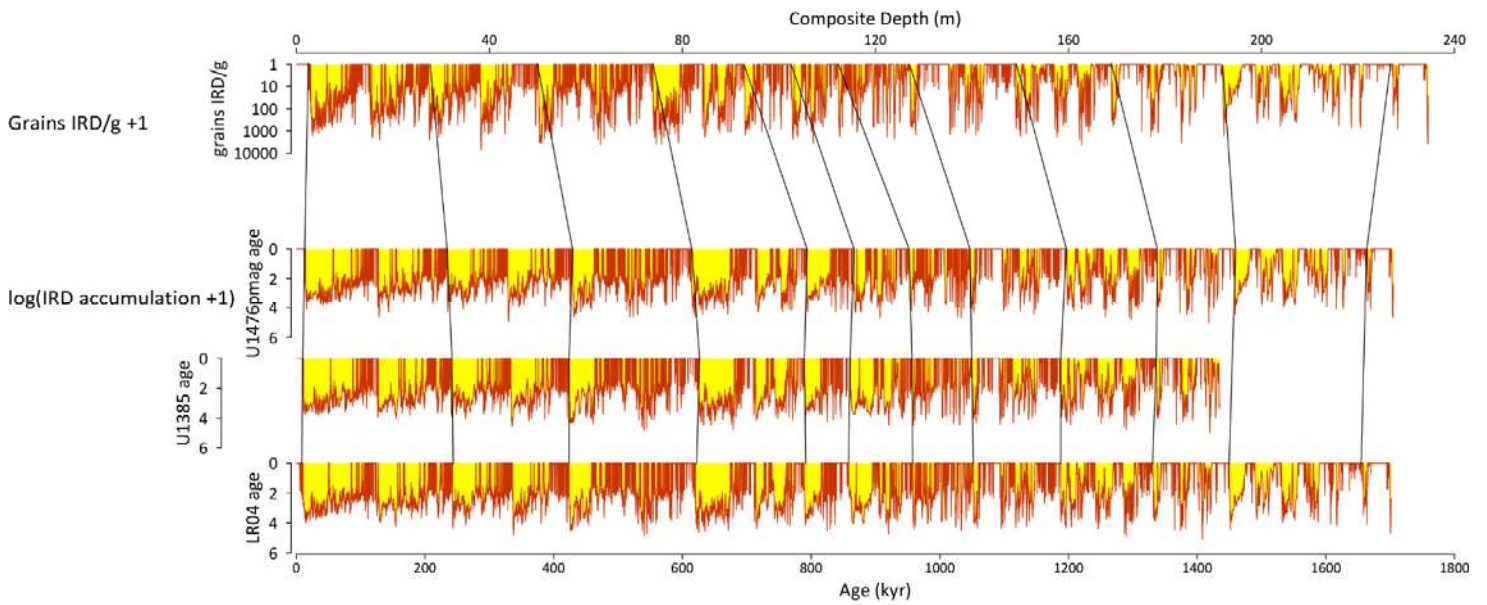
Fig. S5.

Record of IRD grains per gram versus core depth in ODP 983 along with timeseries of IRD accumulation on the 3 age models developed here. Tie-lines are for illustrative purposes only.
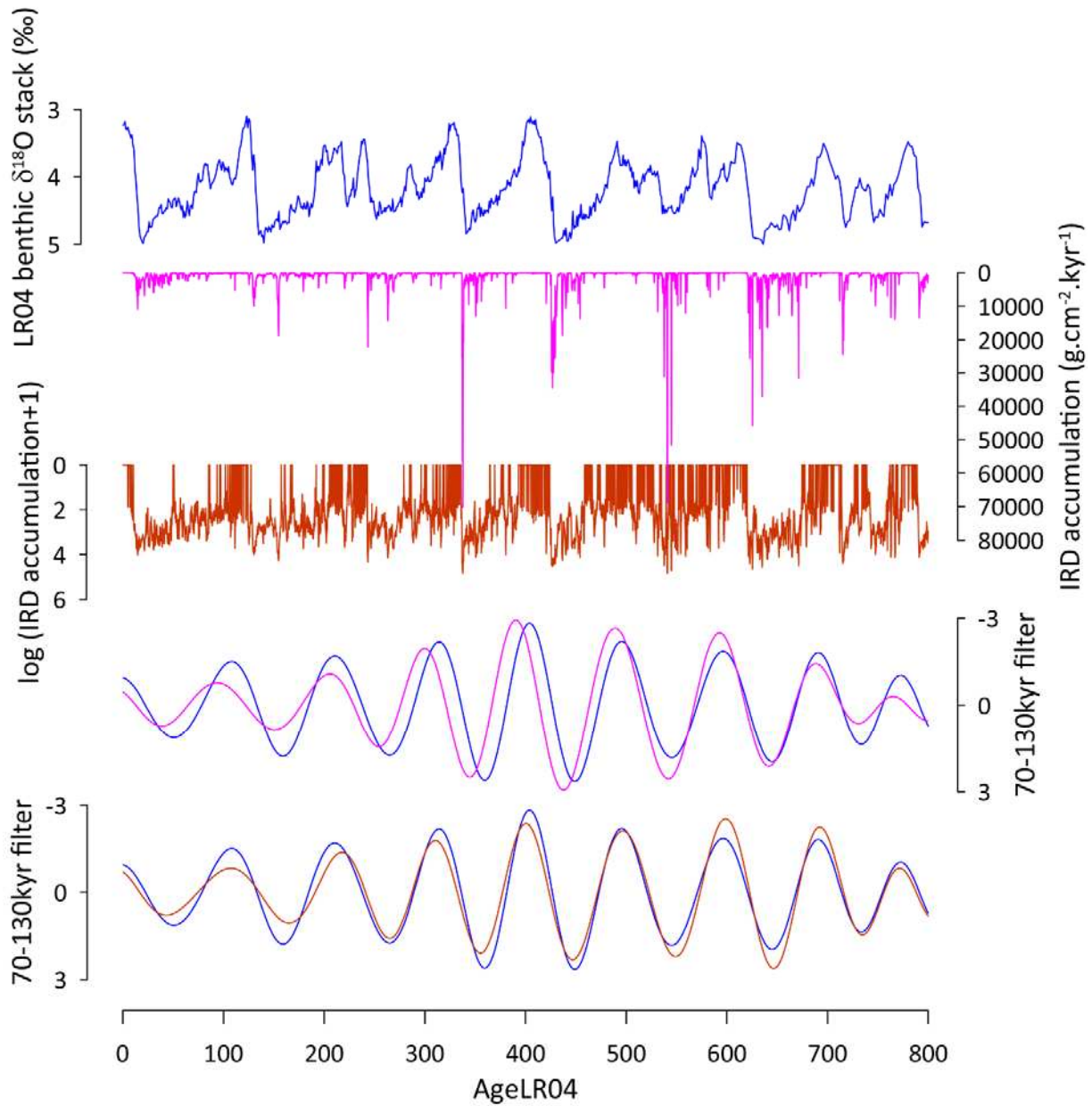
Fig. S6.

Use of log IRD reduces the skew towards deglacial ice rafting events and reveals an in-phase relationship between ice rafting and sea level (LR04) on G-IG timescales. All blue curves represent the LR04 stack, magenta curves are linear IRD and red curves are log IRD.

440
441
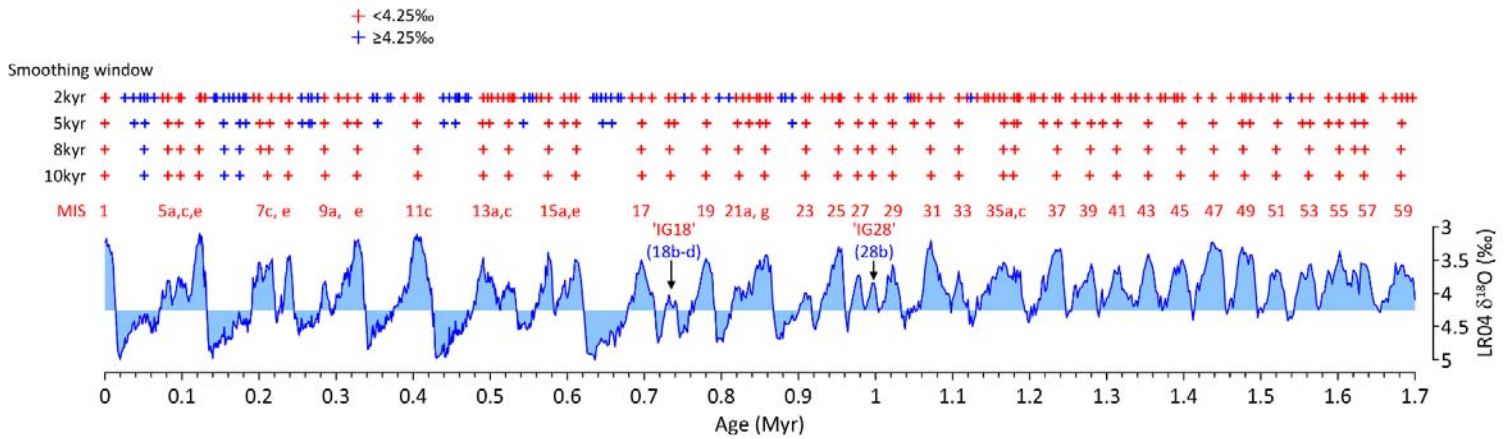
Fig. S7.

Interglacial (IG) events (red crosses) identified as minima in the LR04 benthic $\delta^{18}O$ stack using various smoothing windows. IG18 and IG28 (*12*) are conspicuous minima that have previously been associated with glacial stages 18b-d and 28b respectively (*39*). They are included here because of their conspicuous nature and in order to preserve and include MIS 23. Blue crosses are 'glacial' $\delta^{18}O$ minima (e.g. within MIS 3 and 6) that are excluded by use of a maximum threshold of 4.25‰.

449

450
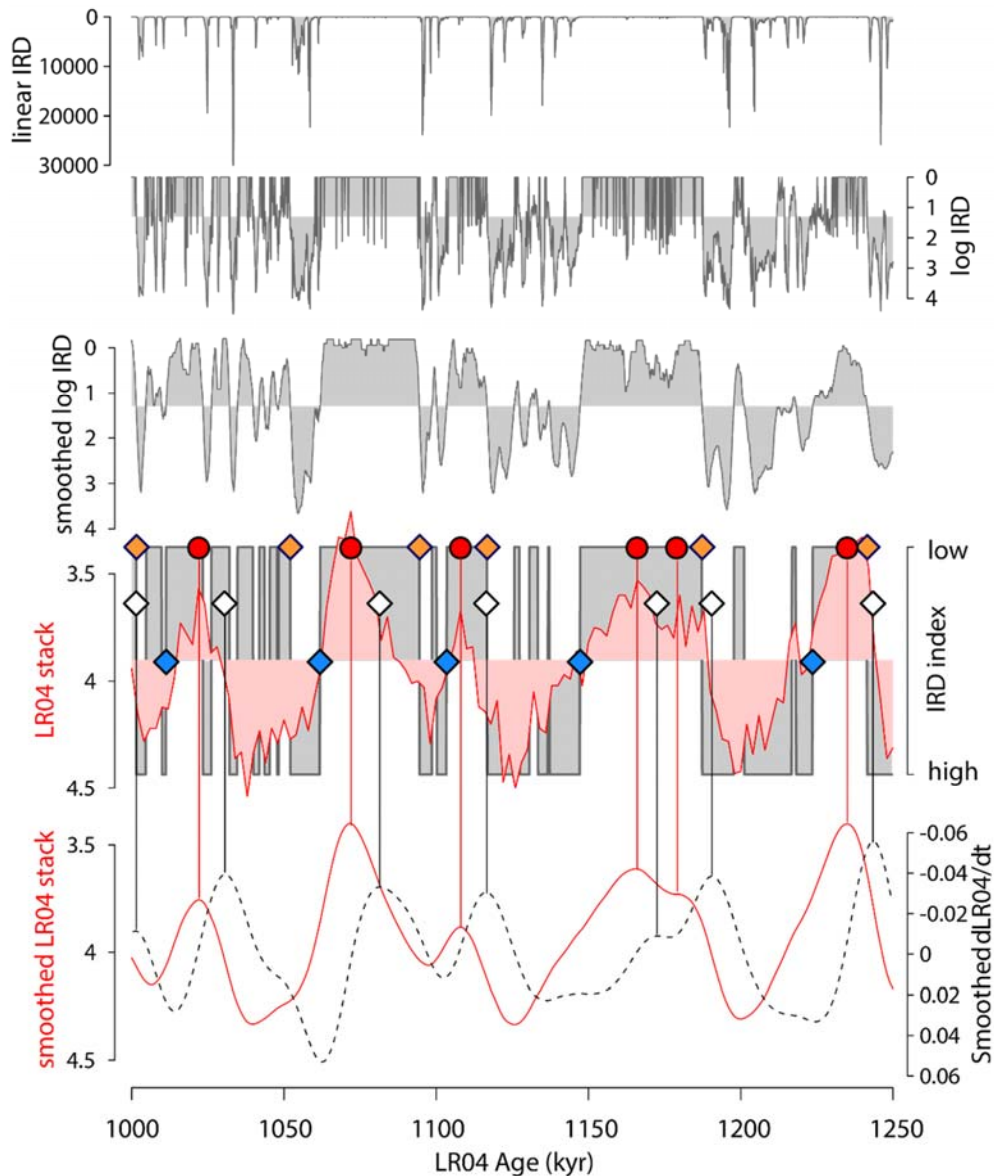
Fig. S8.
Algorithm for assessing the timing of IRD events relative to interglacials and deglacial
transitions as well as minima and maxima in orbital parameters (not shown). From top to bottom:
IRD accumulation from ODP Site 983 on linear and log scales, smoothed (13prm) and detrended
log IRD with threshold for identifying low versus high (significant) IRD (1.3 on log scale
equivalent to 20grains.cm^{-2}.kyr^{-1} on linear scale), IRD index with start (blue diamonds) and end
(orange diamonds) of significant ice rafting according to the algorithm (see supplementary text),
the LR04 stack with interglacials (red circles) and deglacials (white diamonds) identified from
records of smoothed (10kyr) LR04 and smoothed (10kyr) dLR04/dt (bottom). Note that start of
significant ice rafting following an interglacial typically occurs when LR04 has increased to
~3.9‰, which highlights the close relationship between ice rafting at Site 983 and the LR04
stack as an indicator of global ice volume.

463
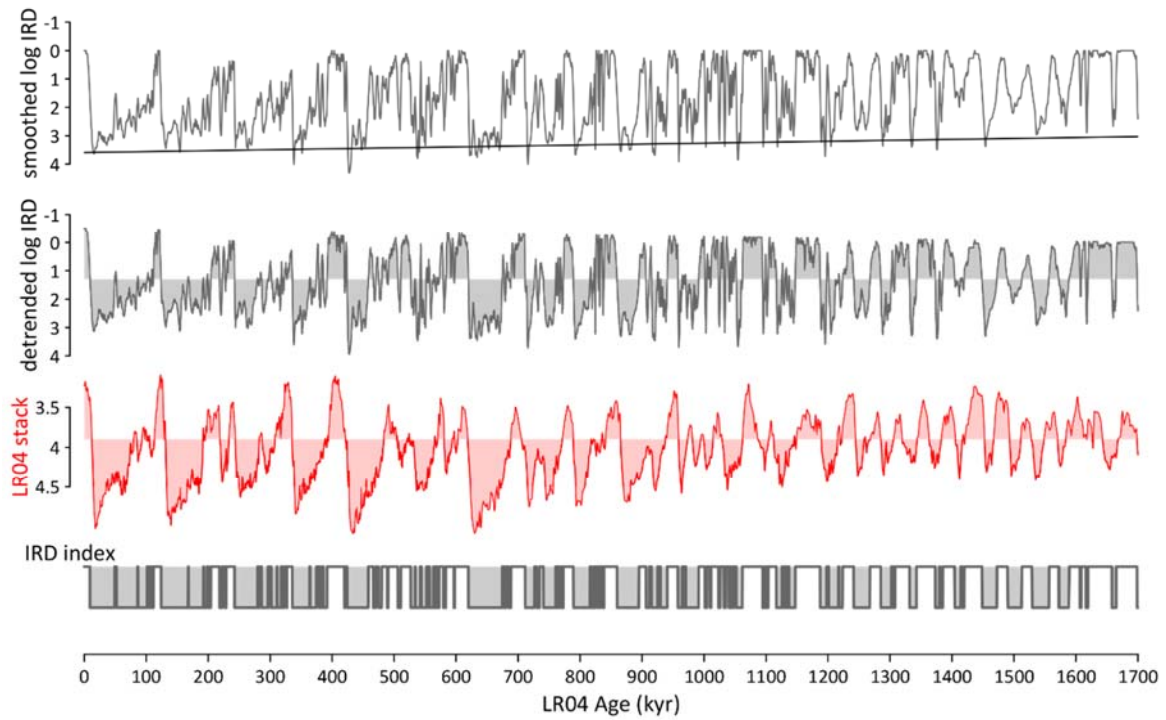
Fig. S9.

Full 1.7Myr IRD index used to identify start and end of significant ice rafting. Upper curve shows 13-point smoothed log IRD and linear trend (0.5/1700kyr) subtracted to produce detrended curve (below). Shaded fill for detrended curve delineates intervals of significant ice rafting (log IRD > 1.3).
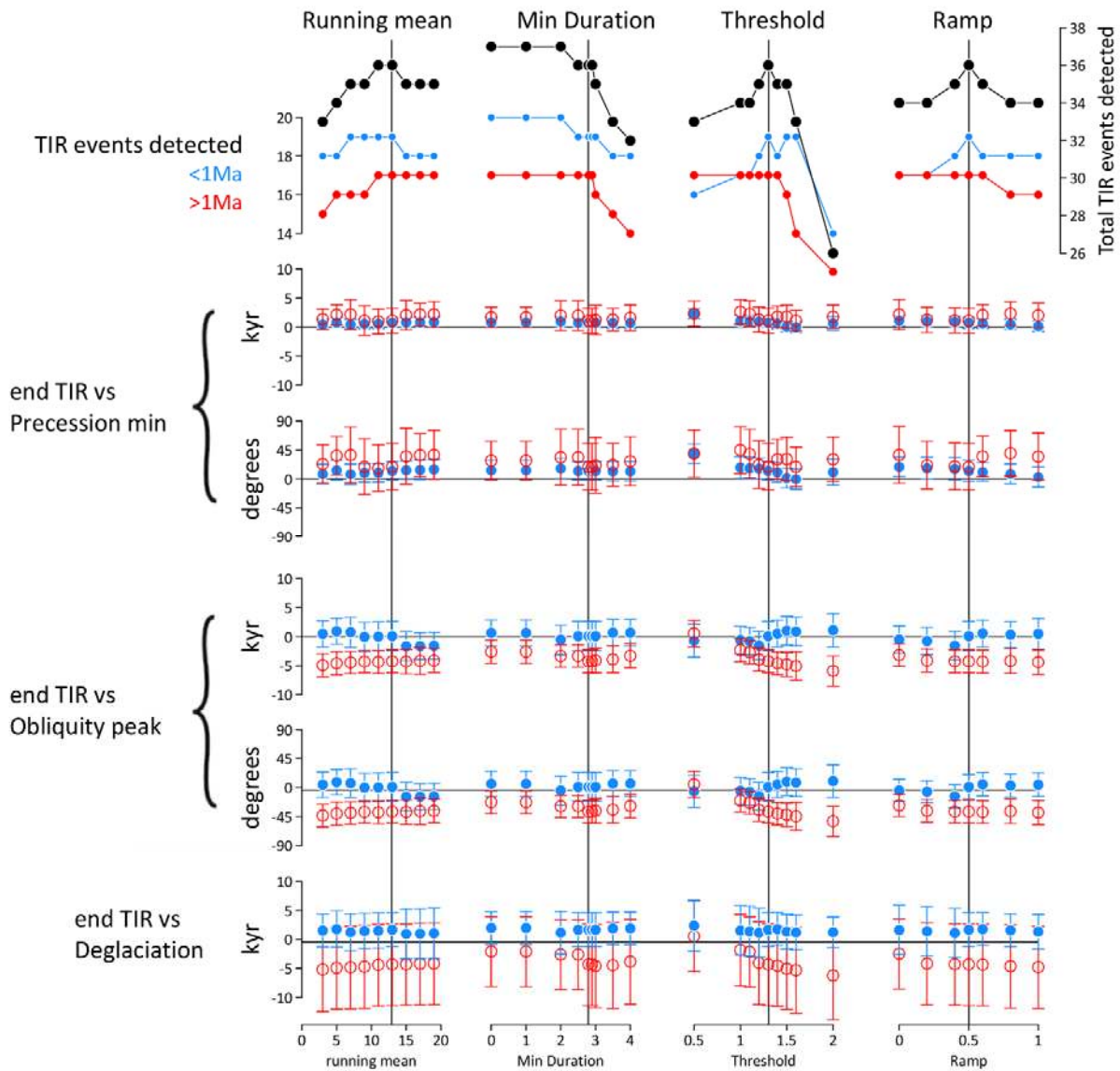
Fig. S10.

Sensitivity analysis for the various parameters used in the IRD algorithm (vertical lines represent implemented values). 'Running mean' is the smoothing applied to the logIRD record prior to construction of the IRD index and 'Ramp' represents detrending the record to account for generally higher levels during the Late Pleistocene. 'Min Duration' is the minimum duration of a TIR event and 'Threshold' is the level above which ice rafting is considered significant. The main conclusions concerning the relative timing of TIR events with respect to orbital peaks and deglaciation as a function of $\delta^{18}O$ are rather insensitive to the choice of parameter value except for very low values of 'Threshold' (see Methods). Error bars in lowermost row represent 1σ, all others represent 80% confidence interval (CI).
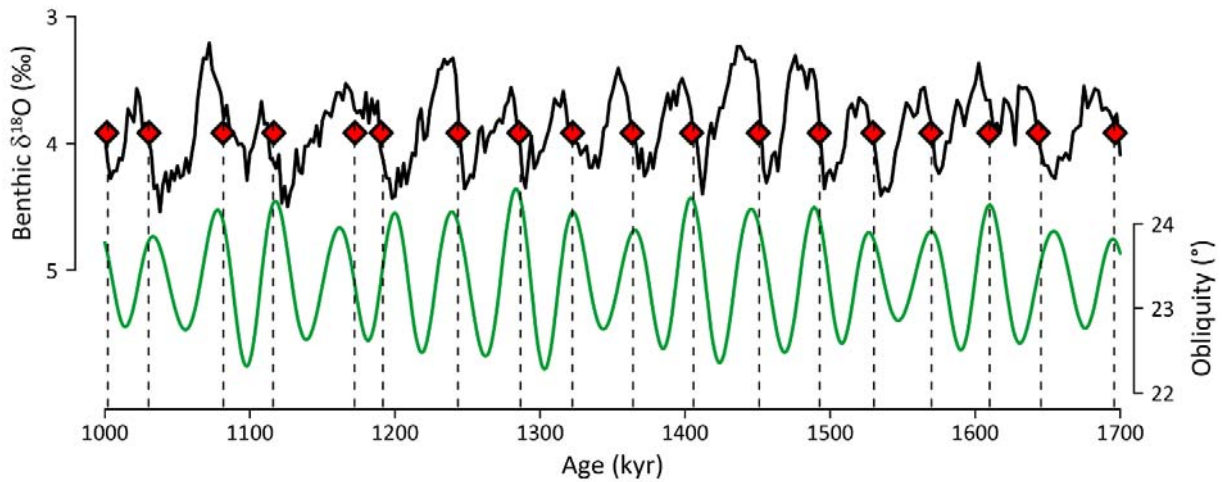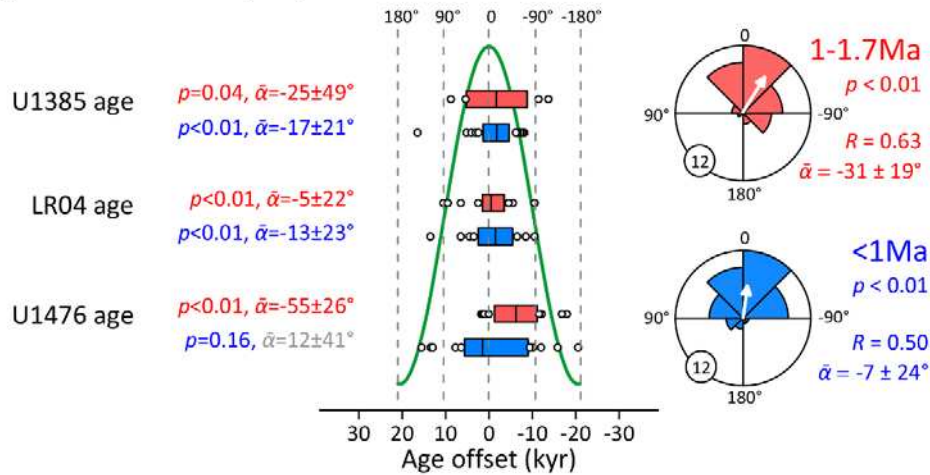
Fig. S11.
Deglacial transitions picked by our algorithm (red diamonds) align closely with rising to
maximum obliquity. This is not surprising for the LR04 age model (which is tuned to obliquity
and precession) but a similar relationship is observed for all three age models employed here.
Box plots for each age model represent median and interquartile range, all other data-points are
shown. Red and blue colors represent pre- and post-1Ma. Rose diagrams combine results from
the 3 age models (see methods): Lower values of *p* suggest higher likelihood of a non-uniform
distribution, *R* is mean resultant vector ($R \rightarrow 1$ as data converge), ᾱ is mean direction with 95%
confidence interval or 80% CI (grey text) for *p*>0.15. Direction of white arrow = ᾱ, length =
R*radial axis. Circled number is length of radial axis.
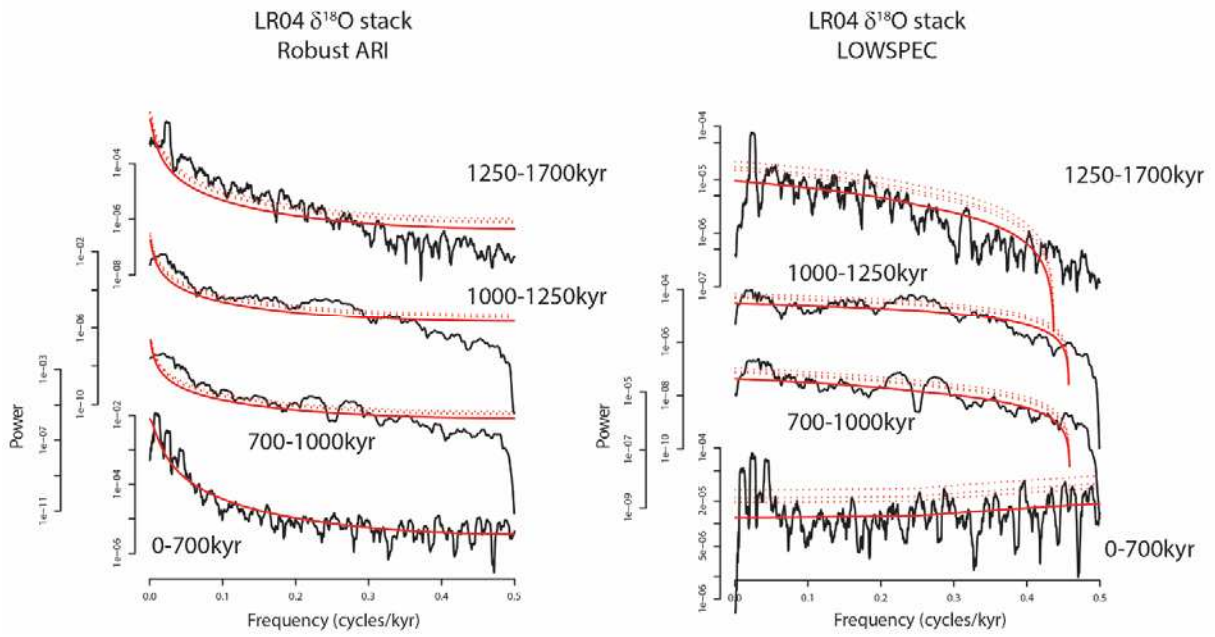
Fig. S12.

Power spectra and red noise estimates out to the Nyquist frequency for the LR04 δ^{18}O stack for 4 times intervals and 2 estimation methods.
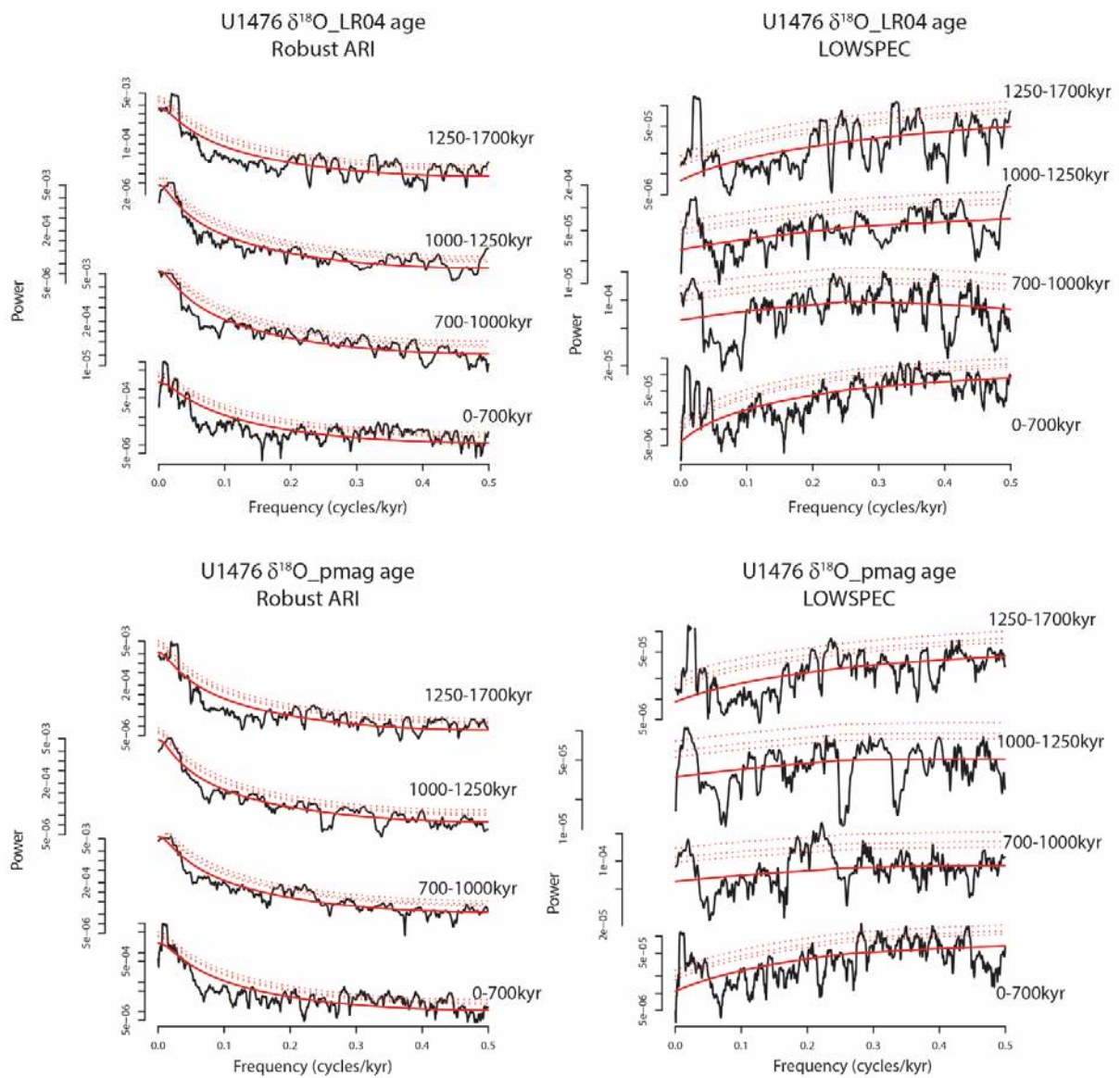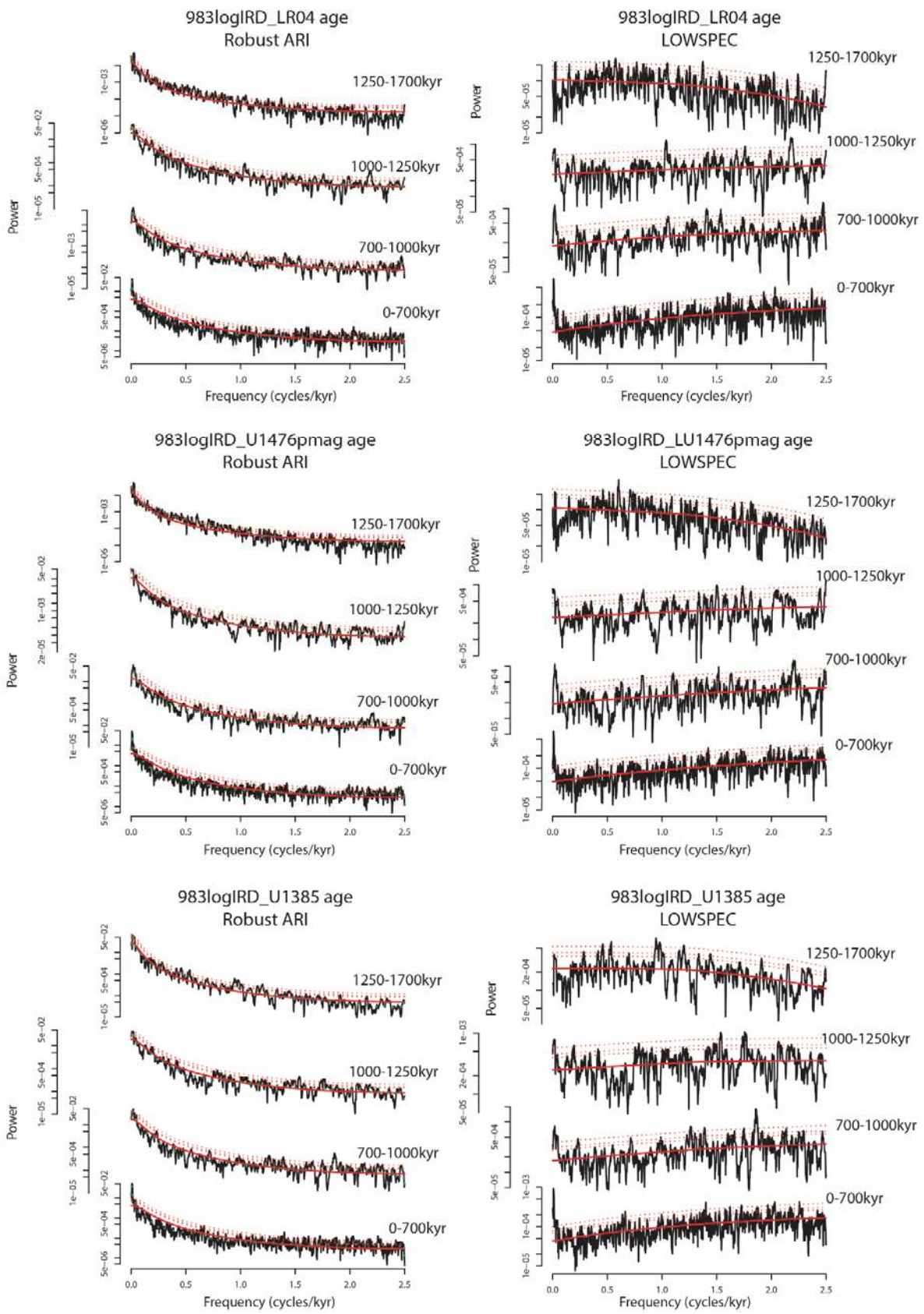
Fig. S13.

Power spectra and red noise estimates out to the Nyquist frequency for the U1476 δ18O record for 4 times intervals, 2 age models and 2 estimation methods.
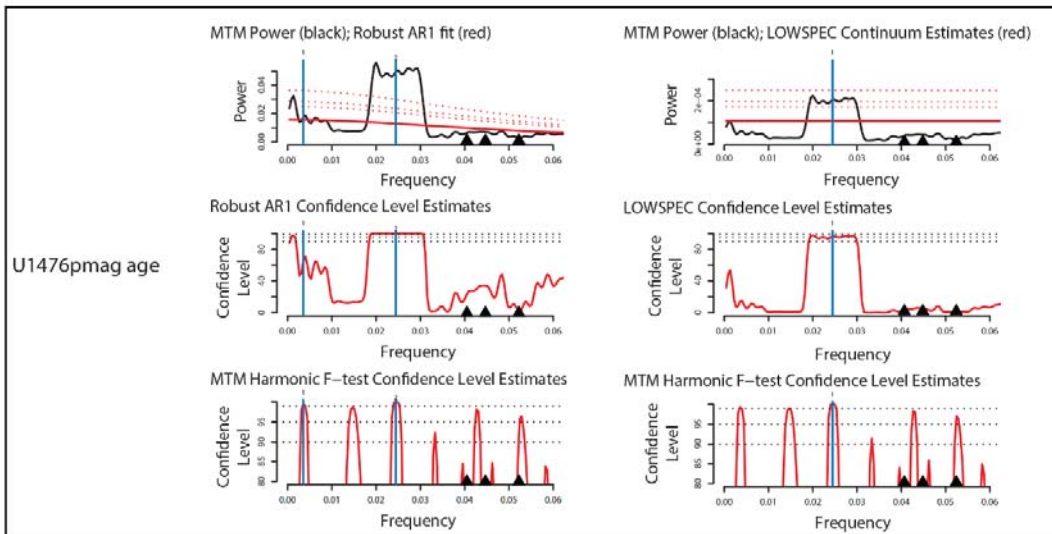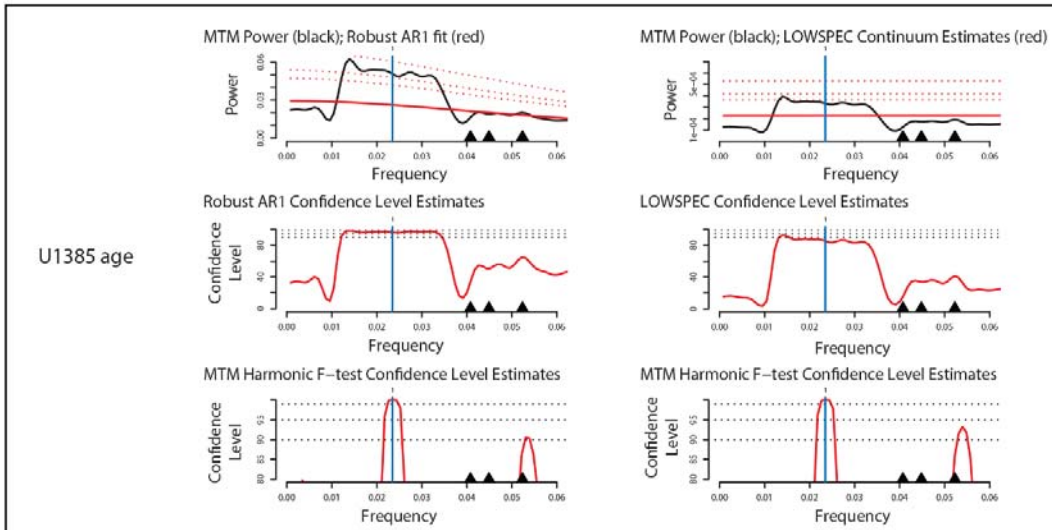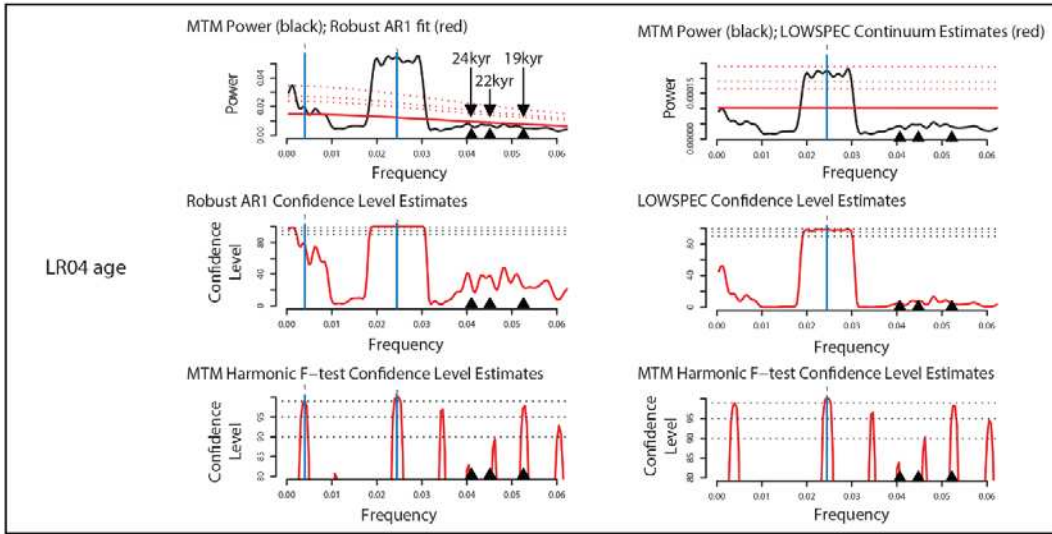
509 **Fig. S14 (previous page).**

510 Power spectra and red noise estimates out to the Nyquist frequency for the logIRD record from
511 ODP Site 983 for 4 times intervals, 3 age models and 2 estimation methods.

512

514 **Fig. S15 (previous page).**

515 Power spectra and red noise estimates out to 0.06 cycles/kyr for the logIRD record from ODP

516 Site 983 for the 1250-1700ka interval, using 3 age models and 3 estimation methods: AR(1),

517 LOWSPEC and a MTM harmonic F-test. Estimated significance within the precession band is

518 below the 90% threshold required to pass the AR(1) and LOWSPEC tests even though modest

519 power is observed with some peaks having relatively high confidence according to the harmonic

520 F-test (see Methods text).

521
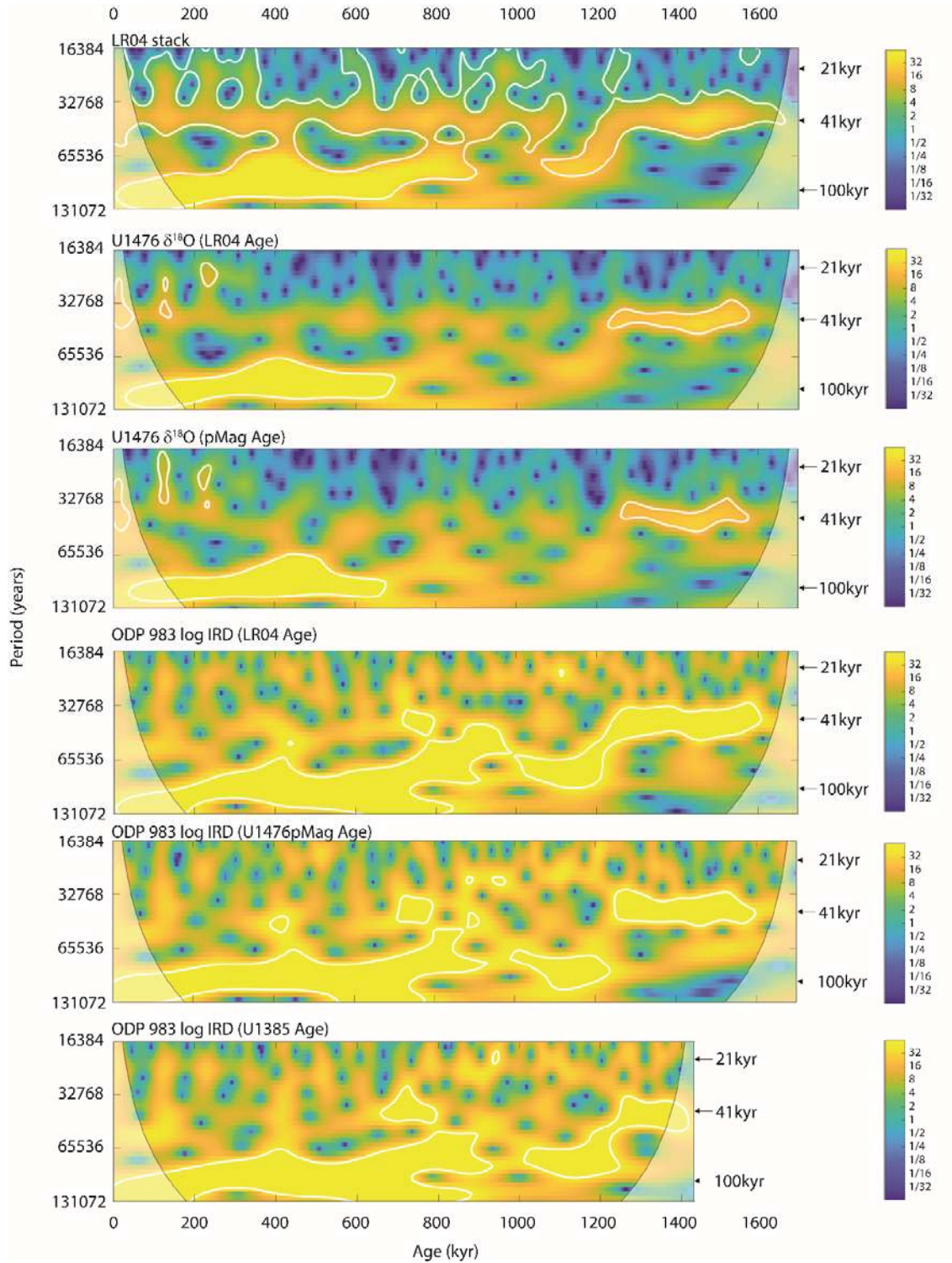
Fig. S16.
Wavelet transforms (*44*) of LR04, U1476 benthic δ^{18}O and ODP 983 log IRD on their various timescales. Yellow colors indicate greater significance. The white contour designates the 5% significance level against red noise and the cone of influence is shown as a lighter shade.

526
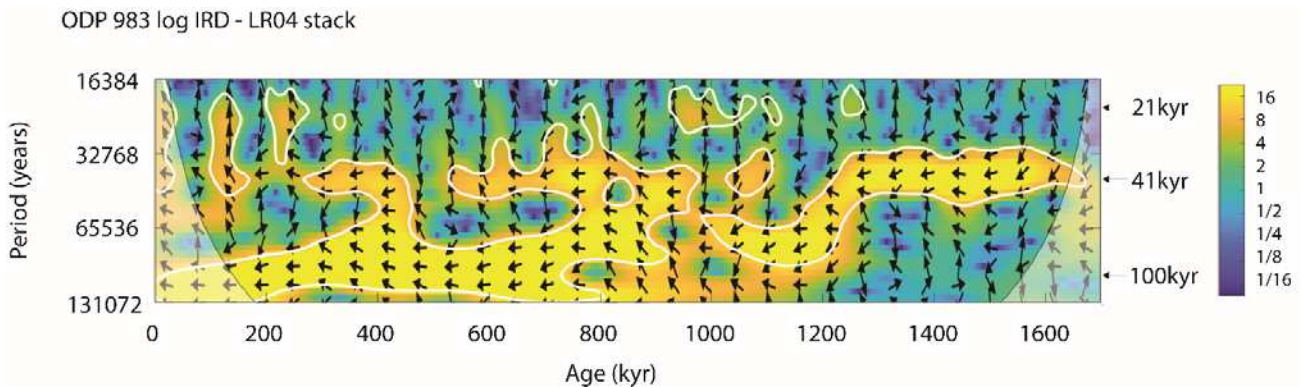
Fig. S17.

Cross wavelet transform (*44*) of log IRD (on its LR04 age model) versus the LR04 benthic $\delta^{18}O$ stack. Yellow colors indicate greater coherence. The 5% significance level against red noise is shown as a white contour. An in-phase relationship is signified by arrows pointing to the left. Note that the significance level may be overestimated as a result of strong power within either of the individual wavelets (as shown in Fig. S16) (*45*).

533

534
535
536

Table S1.

^{40}Ar/^{39}Ar dates (*15*) used to constrain absolute age models pMag and U1476pMag.

539

Event	Depth (ODP 983 Splice)	983 Depth uncertainty (2 sigma)	Depth (U1476 CCSF)	Depth uncertainty (3 sigma; max deviation)	U1476 Depth uncertainty (1 sigma) input for 'Undatable'	^{40}Ar/^{39}Ar Age	Age uncertainty (2 sigma)	Notes
	m	m	m	m	m	kyr	kyr	
Pringle Falls 2	24.49	0.05	4.63	0.01	0.03	212	13	
Bermuda	47.71	0.05	9.06	0.39	0.13	412	3	
La Palma	69.93	0.05	12.66	0.16	0.06	580	8	
Osaka Bay	79.73	0.27	14.58	0.38	0.19	677	22	
Matuyama-Brunhes	90.47	0.40	16.83	0.47	0.25	773	2	
MB precursor	93.11	0.10	17.36	0.04	0.05	795	2	
Kamikatsura	102.73	0.15	19.00	0.05	0.08	867	2	
Santa Rosa	109.27	0.13	20.26	0.06	0.07	927	2	
Top Jaramillo	117.76	0.10				990	4	Excluded from U1476 age model due to ambiguous δ^{18}O correlation
Base Jaramillo	131.76	0.28	22.92	0.71	0.27	1070	3	
Punaruu	138.83	0.10	23.56	0.14	0.07	1126	2	
Top Cobb Mt	147.92	0.15	24.80	0.20	0.10	1186	1	
Base Cobb Mt	151.31	0.13	25.38	0.23	0.10	1221	11	
Bjorn	157.65	0.20	26.27	0.07	0.10	1258	31	
Top Olduvai	247.03	0.20	39.73	0.17	0.11	1787	15	

540
541

542 **Table S2.**

543 Phase relationships and significant (>90% confidence level) periods in the record of log(IRD)

544 from ODP Site 983 versus orbital parameters and deglaciation as a function of benthic $\delta^{18}O$. Red

545 and blue text highlights differences before and after 1Ma.

546

Interval	Phasing						Significant periods (logIRD)		
	'Inception'		'Termination/Deglaciation'				19 - 24kyr	41kyr	80 - 100kyr
	Onset IRD vs obliquity	Onset IRD vs precession	End TIR vs obliquity	End TIR vs precession	End TIR vs deglaciation	Deglaciation vs obliquity			
1-1.7Ma	Decreasing obliquity Fig. 5	N/A Fig. 5	Increasing obliquity Fig. 5	Min precession Fig. 5	Leading or coincident Fig. 6c	Max obliquity Fig. S11	After 1.25Ma Fig. 3	✓ Fig. 3	After 1.25Ma Fig. 3
0-1Ma	Decreasing obliquity Fig. 5	N/A Fig. 5	Max obliquity Fig. 5	Min precession Fig. 5	Coincident Fig. 6c	Max obliquity Fig. S11	✓ Fig. 3	✓ Fig. 3	✓ Fig. 3

547